RESEARCH PAPER

The impact of surface roughness on flow through a rectangular microchannel from the laminar to turbulent regimes

V. K. Natrajan · K. T. Christensen

Abstract Modifications of fluid flow within microscale flow passages by internal surface roughness is investigated in the laminar, transitional, and turbulent regimes using pressure-drop measurements and instantaneous velocity fields acquired by microscopic particle-image velocimetry (micro-PIV). The microchannel under study is rectangular in cross-section with an aspect ratio of 1:2 (depth: width) and a hydraulic diameter of $D_h = 600\,\mu m$. Measurements are first performed under smooth-wall conditions to establish the baseline flow characteristics within the microchannel followed by measurements for two different rough-wall cases [with RMS roughness heights of $7.51\,\mu m$ ($0.0125D_h$) and $15.1\,\mu m$ ($0.025D_h$)]. The roughness patterns under consideration are unique in that they are reminiscent of surface irregularities one might encounter in practical microchannels due to imperfect fabrication methods. The pressure-drop results reveal the onset of transition above $Re_{cr} = 1,800$ for the smooth-wall case, consistent with the onset of transition at the macroscale, along with deviation from laminar behavior at progressively lower Re with increasing roughness. Mean velocity profiles computed from the micro-PIV ensembles at various Re for each surface condition confirm these trends, meaning Re_{cr} is a strong function of roughness. The ensembles of velocity fields at each Re and surface condition in the transitional regime are subdivided into fields embodying laminar behavior and fields containing disordered motions. This decomposition reveals a clear hastening of the flow toward a turbulent state due both to the roughness dependence of Re_{cr} and an enhancement in the growth rate of the non-laminar fraction of the flow when the flow is in the early stages of transition. Nevertheless, the range of Re relative to Re_{cr} over which the flow transitions from a laminar to a turbulent state is found to be essentially the same for all three surface conditions. From a structural viewpoint, instantaneous velocity fields embodying disordered behavior in the transitional regime are found to contain large-scale motions consistent with hairpin-vortex packets irrespective of surface condition. These observations are in accordance with the characteristics of transitional and turbulent flows at the macroscale and therefore indicate that the overall structural paradigm of the flow is relatively insensitive to roughness. From a quantitative viewpoint, however, the intensity of both the velocity fluctuations and structural activity appear to increase substantially with increasing roughness, particularly in the latter stages of transition. These differences are further supported by the trends of single-point statistics of the non-laminar ensembles and quadrant analysis in which an intensification of the velocity fluctuations by surface roughness is noted in the region close to the wall, particularly for the wall-normal fluctuations.

1 Introduction

The characteristics of transitional and turbulent flow in microscale flow passages has received increased attention over the past several years owing to conflicting observations of its physics reported in the literature. While many flow applications at small scales necessarily operate in the laminar regime due to the extremely small length scales involved as well as the friction penalty paid to achieve higher flow rates, there exist many other applications, including microelectronics cooling, refrigeration, and

V. K. Natrajan · K. T. Christensen (✉)
Department of Mechanical Science and Engineering, University of Illinois, Urbana, IL 61801, USA
e-mail: ktc@illinois.edu

mixing in micro-reactors, for example, that leverage the characteristics of transitional and even turbulent flow at these scales. Hence, a complete understanding of these flow regimes at the microscale is required to further improve the design and optimization of microfluidic systems operating under such conditions.

Of particular interest, the results of many past experimental investigations suggest fundamental differences between transition at the microscale and the well-established characteristics of transition at the macroscale. With regard to macroscale transition, Reynolds (1883) first recognized the existence of a critical Reynolds number ($Re \equiv U_b D_h / v$, where U_b is the bulk velocity, D_h is the characteristic diameter, and v is the fluid kinematic viscosity) above which finite amplitude disturbances will grow and lead to the onset of transition from a laminar to a turbulent state. These observations of $Re \cong 2,000$ have since been corroborated in many other studies of macroscale transition along with the recognition that intermittent regions of disordered motions termed turbulent spots bounded by nominally laminar behavior exist in transitional flows with the occurrence and prominence of these spots increasing with Re until a fully turbulent state is eventually attained (Wygnanski and Champagne 1973; Wygnanski et al. 1975; Darbyshire and Mullin 1995, among others). Returning now to observations of transition in microscale flow passages, the experiments of several groups have indicated the onset of transition for fluid flow through microchannels at Re lower than that first established by Reynolds (Peng et al. 1994; Peng and Peterson 1996; Mala and Li 1999; Qu et al. 2000), including for liquid flows in microchannels hundreds of microns in characteristic size (Wang and Peng 1994; Yang et al. 2003; Hsieh et al. 2004; Qi et al. 2007; Ergu et al. 2009, for example) for which the continuum hypothesis is valid and therefore the Navier–Stokes equations should govern the flow physics. In contrast, other microscale studies report the onset of transition near $Re \cong 2,000$ in accordance with macroscale observations (Judy et al. 2002; Qu and Mudawar 2002; Sharp and Adrian 2004; Li and Olsen 2006b). It should be noted, however, that nearly all of these studies simply reported bulk characteristics of the flow (primarily friction factor). As such, the statistical and structural details of the transition process from a laminar to a turbulent state were not captured for complete comparison with the well-established spatial characteristics of this transition at the macroscale. Further, the influence of other effects, like surface roughness and/or cross-sectional geometry, have been largely ignored in many of these microscale studies. Therefore, more comprehensive studies of this physics are needed to ascertain whether the notion of unique transitional flow physics at small scales as proposed in some studies is indeed a possibility.

The recent development of microscopic particle-image velocimetry (micro-PIV) as a tool for acquiring spatially resolved velocity fields at the microscale (Santiago et al. 1998; Meinhart et al. 2000) has sparked significant interest in studying the underlying spatial characteristics of complex flows at the microscale to enhance our understanding of these flows beyond the limited insight bulk measurements can provide. The traditional form of micro-PIV involves the use of ensemble averaging of correlation functions to obtain accurate and well-resolved velocity vector fields in order to alleviate the effects of volume illumination. In this form, however, micro-PIV is inherently limited to the measurement of steady flows or the mean characteristics of unsteady flows (including periodic flows wherein the measurements can be accurately phase locked to the periodic flow physics). In contrast, the accurate measurement of instantaneous unsteady and/or turbulent flow physics requires the acquisition of highly resolved, *instantaneous* velocity fields which demands the use of a relatively high seeding density. In this regard, the first measurements of transition and turbulence via micro-PIV were reported by Li et al. (2005) and Li and Olsen (2006a) for flow through rectangular microchannels where the authors found the onset of transition to occur at Re comparable to that observed at the macroscale. In a complementary study by Li and Olsen (2006b), the authors examined large-scale turbulent structures in rectangular microchannels with varying aspect ratios using spatial correlations of velocity and reported reasonable agreement with macroscale duct-flow data for square microchannels. Likewise, single- and multi-point velocity statistics computed from micro-PIV measurements in the streamwise–wall-normal plane of a 536 μm capillary at $Re = 4,500$ by Natrajan et al. (2007) agreed well with the results of a direct numerical simulation (DNS) of turbulent pipe flow at a comparable Re (Eggels et al. 1994). In addition, Natrajan et al. (2007) reported observations of multiple spanwise vortices (of diameter $\sim 50 \mu m$) aligned in the streamwise direction that formed large scale, inclined interfaces within the instantaneous micro-PIV velocity fields. These characteristics are consistent with the signatures of hairpin vortices and hairpin-vortex packets whose existence in wall-bounded turbulent flows is well-established at the macroscale (Adrian et al. 2000b; Christensen and Adrian 2001; Ganapathisubramani et al. 2003, for example). Therefore, Natrajan et al. (2007) not only established the statistical and structural consistencies of wall turbulence at the micro- and macro-scales, but also validated the efficacy of micro-PIV as a tool for faithfully capturing *instantaneous* flow physics at the microscale.

Recently, Natrajan and Christensen (2007) conducted both pressure-drop and micro-PIV measurements in smooth-wall capillary flow from the laminar to the

turbulent regimes using the same 536 μm capillary utilized by Natrajan et al. (2007). This capillary was chosen for study because its inner surface was found to be extremely smooth (optical profilometry measurements revealed an inner-surface maximum peak-to-valley surface height of 8 nm) which was of critical importance in order to eliminate surface roughness as a possible culprit for transition at anomalously low Re as many studies have previously reported. Natrajan and Christensen (2007) reported the onset of transition at $Re \simeq 1,900$, with fully turbulent flow observed at $Re \simeq 3,400$, consistent with the aforementioned characteristics of macroscale transition. Further, examination of the instantaneous velocity fields acquired by micro-PIV revealed that transitional flows at the microscale are composed of a subset of velocity fields that reflect laminar flow and a fraction that capture significant deviation from laminar behavior (i.e., disordered motions) with the latter fraction increasing with Re. Again, these observations are entirely consistent with a growing number of turbulent spots bounded by regions of laminar flow as is established in the literature on macroscale transition (Wygnanski and Champagne 1973; Wygnanski et al. 1975; Darbyshire and Mullin 1995). Of particular interest, the instantaneous velocity fields embodying disordered motion often contained multiple spanwise vortices aligned in the streamwise direction with these vortices collectively inducing ejections of low-speed fluid away from the wall which generate elongated regions of streamwise momentum deficit below the inclined interfaces formed by the spanwise vortex cores. Strikingly similar to the observations of Natrajan et al. (2007) for turbulent flow in the same capillary, these spatial characteristics are entirely consistent with hairpin-vortex packets that populate wall-bounded turbulent flows at the macroscale. The existence of hairpin-vortex organization within turbulent spots in transitional flows is further supported by recent multi-plane stereo-PIV measurements conducted in the interior of spots in a macroscale flat-plate boundary layer by Schröder and Kompenhans (2004). Finally, Natrajan and Christensen (2007) reported that the single-point statistics of the non-laminar ensembles, including profiles of the mean streamwise velocity, RMS streamwise and wall-normal velocities, σ_u and σ_v, and the Reynolds shear stress (RSS), $-\langle u'v' \rangle$, support a gradual progression of the flow toward a fully turbulent state with increasing Re. In a follow-up effort, Natrajan and Christensen (2009a) used quadrant analysis to show that the maturation of the flow toward a turbulent state is accompanied by an increase in the intensity of the instantaneous RSS-producing events that shift closer to the wall with increasing Re. In addition, this study also identified the pivotal role of large-scale hairpin packet motions in the transport of both kinetic energy as well as Reynolds shear stress in wall-bounded transitional flows at the microscale.

With regard to surface roughness, its impact on flow within microscale flow passages is not well-understood yet it represents a significant challenge because most methods of flow-passage fabrication at these small scales leave behind surface irregularities that could significantly alter fluid flow compared to smooth-wall conditions. In general, surface conditions that would behave hydraulically smooth at the macroscale because of the broad separation between the scale of the roughness (ϵ; often taken to be the root-mean-square (RMS) roughness height, k_{rms}) and the hydraulic diameter of the flow passage (D_h) may significantly affect the flow if employed in a microscale flow where the relative roughness, ϵ/D_h, increases significantly due to a decrease in D_h. In the aforementioned studies reporting deviation from macroscale behavior, surface roughness was either cited as a possible culprit for or may have played an unwitting, yet defining, role in triggering an early transition to turbulence at low Re. Unfortunately, many of these studies reported little regarding the surface quality of the passages under study, though Morini (2004) argued that surface roughness, in conjunction with the secondary-flow behavior associated with flow passages of non-circular cross-section, may indeed account for some of these conflicting observations. Further, beyond the impact of roughness on the initiation of transition at lower Re, understanding its influence on momentum-transport characteristics in the transitional and turbulent regimes at the microscale is critical because any deviations from smooth-wall behavior would subsequently impact how one models such flows, including their heat-transfer characteristics, for example. In this regard, pressure-drop measurements performed for flow through rough-wall microchannels by several groups indicate onset of transitional behavior at Re far lower than that expected for smooth-wall flow (for instance, Wu and Little 1984; Mala and Li 1999; Pfund et al. 2000; Liu et al. 2007, among several others). Recently, Kandlikar et al. (2005) conducted a more systematic study of the effects of surface topography on flow behavior at the microscale by performing a series of pressure-drop measurements across microchannels with sawtooth roughness elements that were arranged in both aligned and offset configurations. Based on their measurements for relative roughness values in the range $0.06 \leq \epsilon/D_{h,cf} \leq 0.14$, the authors proposed the use of a constricted-flow diameter, $D_{h,cf}$ ($=D_h - 2\epsilon$, where ϵ was taken to be the average height of the roughness element), and showed that the friction factor for flow through rough-wall microchannels can be adequately predicted by classical laminar flow theory when the hydraulic diameter, D_h, is replaced with the constricted-flow diameter, $D_{h,cf}$. Nevertheless, these experiments revealed initiation of

transition at $Re = 800$ and 350 for air and water, respectively. Hao et al. (2006) studied the flow of water through smooth- and rough-wall (discrete rectangular elements) microchannels using micro-PIV. Based on profiles of the mean and RMS streamwise velocities, the authors concluded that transition to turbulence is initiated at $Re \approx 900$ in microchannels with relative roughness heights of $\epsilon/D_h = 0.26$ and 0.32. However, it should be noted that these values of relative roughness are well beyond those due to surface defects associated with manufacturing and are more representative of "flow blockage."

Given the lack of consensus regarding how surface roughness alters momentum transport at the microscale, the goal of the current effort is to document the underlying characteristics of microscale wall-bounded flow in the presence of surface roughness. To this end, both micro-PIV and pressure-drop measurements are performed for flow through a rectangular 1:2 aspect ratio (depth: width) microchannel of $D_h = 600\,\mu m$ over a broad range of Re spanning the laminar, transitional and turbulent regimes. These measurements are first performed for flow through a smooth-wall rectangular microchannel in order to determine how a flow passage of non-circular cross-section might alter the transitional flow characteristics described earlier for flow through a smooth circular capillary (Natrajan and Christensen 2007). Following this, pressure-drop and micro-PIV measurements are performed for flow through rough microchannels with two different roughness conditions (one of twice the magnitude of the other) on two of the four microchannel walls to facilitate optical access for micro-PIV. The roughness under consideration is unique in that it contains a broad range of topographical scales and is therefore more representative of the random surface defects that one would likely encounter in industrial microchannels due to imperfect fabrication methods. This data is used to contrast the statistical and structural characteristics of flow through the smooth- and rough-wall microchannels as well as assess the impact of increased surface irregularities as the flow transitions from a laminar to a turbulent state.

2 Experiments

Figure 1a, b shows schematics of the common test section employed for all of the experiments outlined herein. This microchannel testbed consists of three parts, a base and two side-wall inserts, with the base formed from a $306 \times 11 \times 7.9$ mm block of oxygen-free copper that acts as the foundation of the device. This block is machined using a
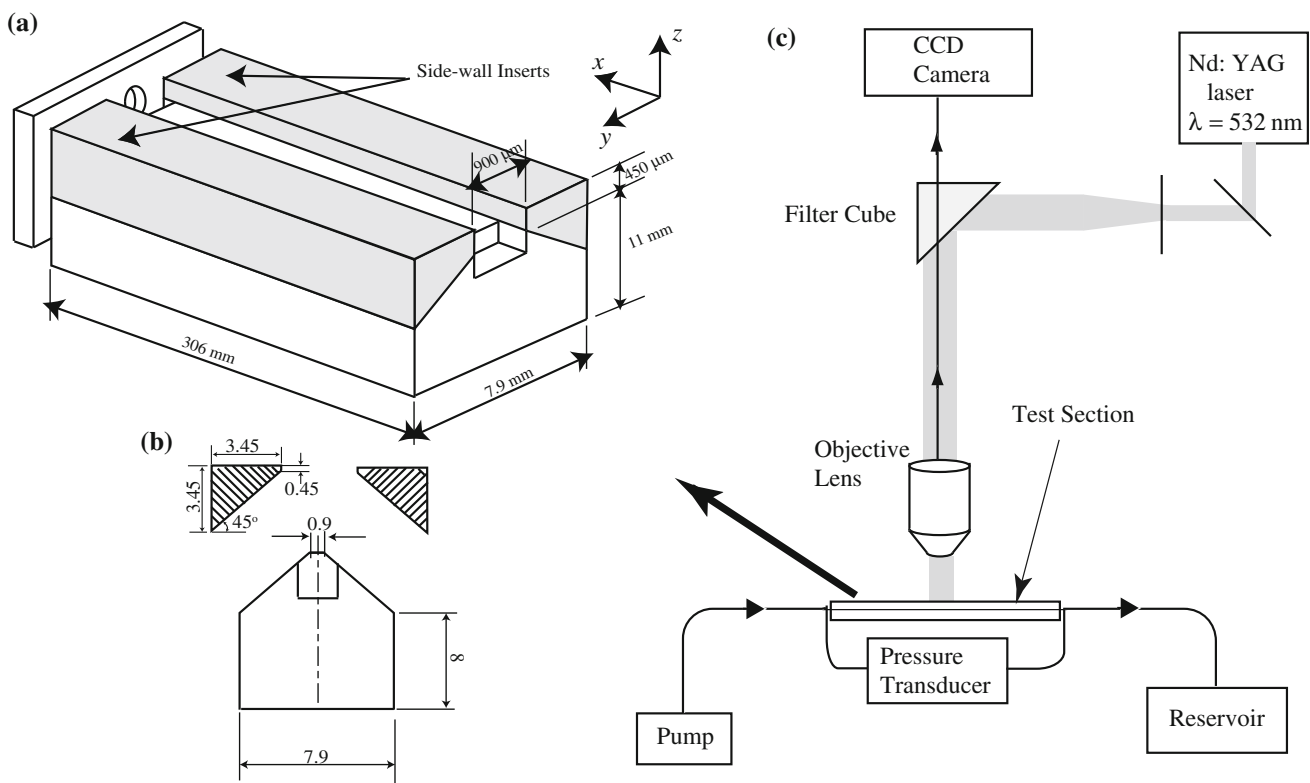
Fig. 1 a Schematic of the microchannel test rig. **b** Cross-sectional view of the base and the two side-wall inserts that contain the bottom and the vertical faces of the rectangular microchannel, respectively. **c** Schematic of the experimental setup for the micro-PIV measurements. *Note*: Dimensions in parts (**a**) and (**b**) are not to scale

jeweler's saw on a CNC machine so that its top surface has a rectangular cross-section in the x–y plane (width = 900 µm, length = 306 mm) and this surface is polished to achieve smooth surface conditions (optical profilometry measurements indicate an RMS surface roughness of 90 nm). This surface forms the bottom wall of the rectangular microchannel and is common to all of the surface conditions studied herein. On either side of the top face of the base is an inclined surface (inclined at an angle of 45° to the x–z plane), along which a side-wall insert is placed and attached to the base by means of 0–80 (1/8 in.) flathead screws spaced at 50-mm intervals along the length of the test section (Fig. 1b). The inclined surfaces are first coated with a thin layer of thermal grease in order to minimize the thermal resistance at the interface between the base and side-wall inserts for complementary heat-transfer studies reported in Natrajan and Christensen (2009b, c). Following this, the side-wall inserts (shaded in gray in Fig. 1a) are mounted on the inclined faces on either side of the bottom wall of the microchannel so that their vertical faces (height = 450 µm and length = 306 mm in the x–z plane) form the side walls of the rectangular microchannel. Finally, in order to provide optical access to the interior of the microchannel, the top of the assembled test section is sealed with glass slides along its entire length. The glass slides are first spin-coated with a 12−µm thick layer of PDMS and are then placed on the top surface of the assembled test section with the PDMS-coated sides facing down. Upon curing the PDMS at a temperature of 80° C, it forms a strong bond with copper and thereby seals the test section. The resulting microchannel formed by this assembly method has a rectangular cross-section of length = 306 mm, width = 900 µm, and height = 450 µm which yields $D_\mathrm{h} = 600$ µm to within 2 µm (0.33%). Of particular significance, this microchannel allows for varied side-wall surface conditions to be tested by simply replacing the side-wall inserts while the top and bottom surfaces of the microchannel remain unchanged. A similar test section, wherein the boundary conditions were varied using side-wall inserts, was employed by Kandlikar et al. (2005) in order to examine the effects of surface roughness on pressure drop in single-phase minichannel flows.

Ensembles of instantaneous velocity fields are acquired in the streamwise–wall-normal (x–y) plane at center depth in the z direction by micro-PIV at multiple Re for laminar, transitional, and turbulent flow through the microchannel testbed fitted with the smooth and the rough side-wall inserts. For the current effort, deionized water is chosen as the working fluid and its flow through the test section is driven by a gear pump (115 VAC console digital dispensing drive and 0.084 ml/rev suction shoe gear pump head, Cole Parmer). All instantaneous velocity fields are acquired at the streamwise location $x = 500D_\mathrm{h}$, where the

flow is assured to be fully developed at all Re studied herein. All PIV measurements are conducted at times beyond the transient start-up of $t < 7$ s, where the flow rate is found to be steady to within ± 1.7% of the desired flow rate that is set using the gear pump. Finally, the pressure drop, ΔP, across the test section is monitored with a differential pressure transducer (Validyne DP-15-40) and a demodulator (Validyne CD-15) to within ± 2%.

The instantaneous two-dimensional velocity (u, v) fields are acquired by micro-PIV across the width of the rectangular microchannel with a field of view of $2.9W \times 2W$ in the streamwise–wall-normal plane passing through center-depth of the rectangular microchannel ($W = 450$ µm is the half-width of the microchannel). This region of the flow is of interest because it allows the impact of roughness on the flow in the direction of mean flow (x) as well as the direction normal to the two rough side walls (y) to be discerned. The field of view is volume-illuminated with a double-pulsed Nd:YAG laser ($\lambda = 532$ nm, Continuum) whereby each beam is directed through an epi-fluorescent filter cube via an entry port in the rear of the microscope (Olympus BX60) followed by passage through a $10 \times$ (N.A. = 0.30) objective lens that guides the light to the test section. The flow is seeded with 1 µm fluorescent (Nile red) particles (Molecular Probes) that are efficiently excited by the second-harmonic (green) emission of the Nd:YAG laser and have a peak emission at $\lambda = 575$ µm. The emission from the particles passes through the filter cube while the incident wavelength is blocked, ensuring only the fluoresced light from the particles is imaged by the $2k \times 2k$ pixel, 12-bit frame-straddle CCD camera (TSI 4MP). The seeding density of the tracer particles is optimized to a volume fraction of 0.039% in deionized water by taking into account the depth of correlation due to volume illumination [$\Delta z = 15.2$ µm using the methodology of Olsen and Adrian (2000)]. The time delay between two successive images in a pair is adjusted at each Re to yield bulk particle displacements of roughly eight pixels so that the relative instantaneous velocity measurement uncertainty due to random errors in estimation of the sub-pixel displacement is approximately 1.5% (Prasad et al. 1992; Christensen and Adrian 2002). The micro-PIV images are interrogated using two-frame cross-correlation methods with 56^2-pixel first windows and larger 64^2-pixel second windows that are offset by eight pixels in the streamwise direction. The first interrogation windows are overlapped by 50% to satisfy Nyquist's sampling criterion which results in vector grid spacings of $\Delta x = \Delta y = 11.9$ µm in both spatial directions. The instantaneous vector fields are then validated using standard deviation and local magnitude difference comparisons to remove erroneous velocity vectors. The few holes (< 3%) generated by this process are filled either with alternative velocity choices

determined during the interrogation or interpolated in regions where at least 50% of neighbors were present. Each instantaneous vector field is then low-pass filtered with a narrow Gaussian filter to remove any noise associated with frequencies larger than the sampling frequency of the interrogation.

With regard to uncertainty in the present micro-PIV velocity measurements, bias errors due to peak locking are minimal since the present particle-image diameters exceed two pixels (Westerweel 1997; Christensen 2004) as are bias errors due to loss of particle-image pairs since a larger second interrogation window is employed with a discrete window offset in the flow direction. Thus, the uncertainty in the present instantaneous velocity measurements is approximately 1.5% due to the aforementioned uncertainty in sub-pixel estimation. Since this error is random, its impact on the statistics presented herein is muted considerably by first averaging over each ensemble of at least 800 instantaneous and statistically independent velocity realizations per case (each Re and surface condition) followed by averaging over 100 data points per field in the homogeneous streamwise direction to yield statistical profiles that are a function of the inhomogeneous wall-normal direction (y). As such, each statistical data point presented is derived from the averaging of over 80,000 statistically independent samples. Therefore, the impact of the 1.5% uncertainty in instantaneous velocity is reduced by at least two orders of magnitude and symbol size is therefore representative of the maximum uncertainty in each statistic.
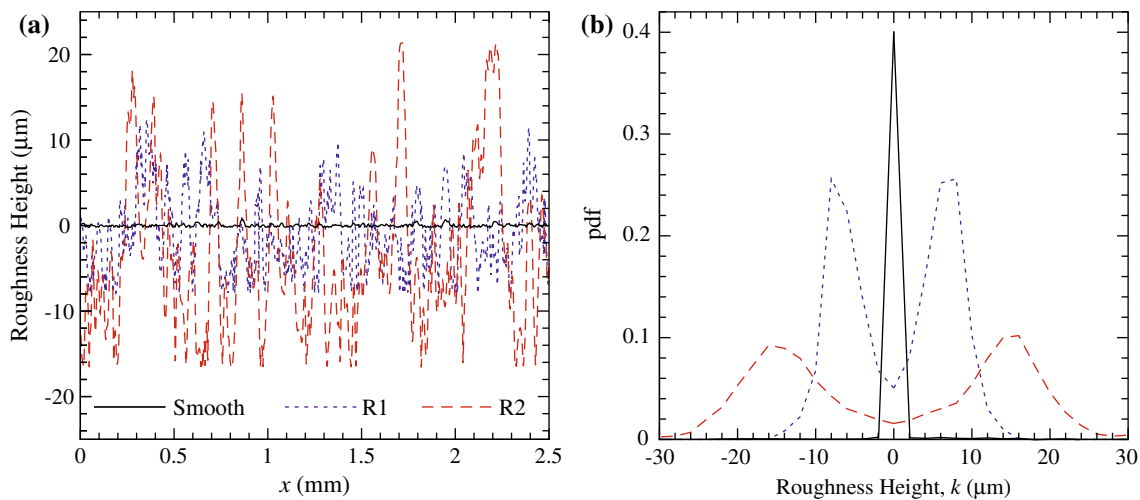
3 Characterization of surface roughness

As described above, the impact of various surface irregularities on fluid flow at the microscale can be studied by varying the surface texture of the $450\,\mu m \times 306\,mm$ vertical faces of the two side-wall inserts of the microchannel testbed. It should be noted, therefore, that the upper and lower walls of the microchannel remain smooth in all experiments while the surface conditions of the vertical walls are varied. Three different surface conditions are the subject of the present contribution: smooth side walls and two different rough side-wall cases (referred to herein as the R1 and R2 cases). For the rough-wall cases, new side-wall inserts are manufactured and their vertical faces are textured by sandblasting using $60\,\mu m$ silica particles exiting from an air gun. The exposed surface, upon impact with the silica particles, develops a highly irregular, grainy surface texture that serves as the roughness pattern for the current effort. *It should be noted that we have specifically chosen not to consider the impact of carefully patterned roughness (well-defined surface elements arranged along*

the surfaces at a fixed wavelength, for example) since such idealized surface elements do not faithfully mimic the surface characteristics one would likely encounter due to fabrication imperfections. Rather, the intent herein is to provide data on fluid flow that is relevant to the accurate representation of such processes in industrially manufactured microchannels for which surface roughness is likely present and simply due to manufacturing imperfections as opposed to carefully designed surface texturing.

In order to ensure homogeneity in the average characteristics of the roughness generated along the axial length of the side-wall inserts, the inserts are placed on a fixture, that is, then attached to a translation stage with the surfaces to be roughened facing vertically upwards. During the sandblasting process, the air gun is fixed 8 cm above the surfaces while the translation stage traverses the surfaces past the particle-laden jet emitted by the air gun at a constant pace of 1.2 cm/s. Such an procedure is meant to ensure consistency in the roughness patterns generated all along the length of the test section. Finally, detailed preliminary tests of this protocol indicate that the average spatial characteristics of the roughness generated by the sandblaster in this manner is a strong function of the number of passes a given surface makes past the fixed air gun [i.e., $\epsilon = fcn(\# \text{ of passes})$]. For the two roughness conditions presented herein, R1 and R2, 7 and 50 passes, respectively, are utilized to generate these two surface conditions.

Figure 2a shows representative line traces of the surface profiles measured by a surface profilometer (Sloan Dektak ST) with a resolution of 0.1 nm for all three surface conditions. For reference, 10 different one-dimensional (1D) traces in the axial direction were made at different axial locations along the 306-mm length of the side-wall inserts for each surface condition. The traces in Fig. 2 provide a measure of free of defects in the smooth-wall inserts (recall the smooth-wall case was not roughened by the sandblaster but rather polished after machining), while also illustrating the enhanced surface roughness of the R2 case compared to the R1 case due to the increased number of passes by the particle-laden jet of the air gun. A more quantitative measure of these surface conditions is shown in Fig. 2b, which represents probability density functions (pdfs) of the roughness amplitudes about the mean surface elevation computed from all 10 independent samples per surface condition. As documented in Table 1, the smooth case has a maximum peak-to-valley roughness height of 197 nm (0.033% of D_h) and a RMS roughness height, k_{rms}, of 92 nm (0.015% of D_h). These weak variations in the surface character are clearly evident in the smooth-wall pdf in Fig. 2b as its peak, which is centered at zero, is quite narrow. In contrast, the surfaces R1 and R2 have RMS roughness heights of 7.52 and 15.1 μm (1.25 and 2.51% of

Fig. 2 **a** Representative line traces of surface roughness measured profilometry. **b** Pdfs of the roughness heights for the smooth and the rough surfaces

**Table 1** Average characteristics of the smooth and the rough-wall surfaces

Surface	k_{rms} (μm)	Max. P–V roughness height (μm)	k_{rms}/D_h
Smooth	0.09	0.2	0.00015
R1	7.51	40.4	0.0125
R2	15.1	71.8	0.0251

D_h), respectively, and maximum peak-to-valley roughness heights of 40.4 and 71.8 μm (6.73 and 11.97% of D_h), respectively. These surface irregularities are at least two orders of magnitude more substantial than the smooth case and the pdfs for the R1 and R2 cases also reveal significant differences from the smooth case, with each displaying a nearly symmetric, bimodal distribution about zero with peaks centered at roughly $\pm k_{rms}$ for each case. As such, the roughness-generation method utilized herein results in rough surfaces containing broad ranges of topographical scales with similar numbers of surface valleys and peaks about the mean elevation in both the R1 and R2 cases. These pdfs therefore support the notion that the mean hydraulic diameter of the R1 and R2 cases is the same as the smooth-wall case since the roughness studied herein does not alter the location of the mean elevation of the side-wall inserts in either of the roughness cases.

4 Results

4.1 Pressure-drop measurements

In order to document the flow behavior within the smooth- and the rough-wall microchannels, particularly the *Re*
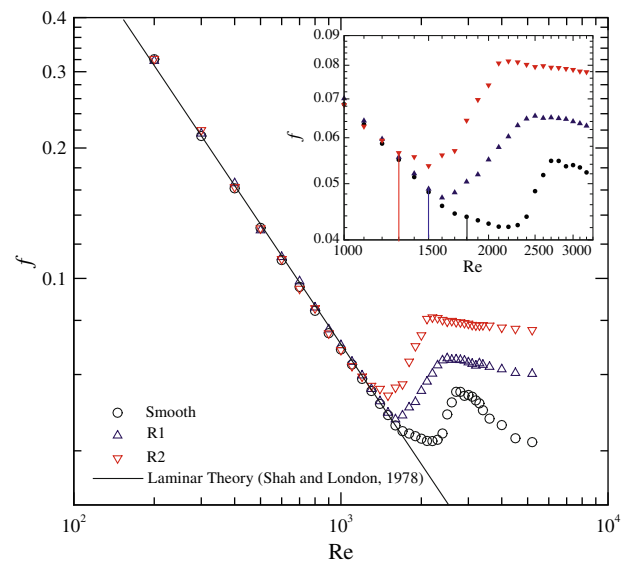
Fig. 3 Friction factor as a function of *Re* for flow through the smooth- and rough-wall microchannels

ranges for which laminar, transitional, and turbulent flow should be expected, measurements of the pressure drop, ΔP, across the length of the microchannel, L, are conducted for $100 < Re < 5{,}200$ in increments of 100. Figure 3 shows the Reynolds-number variation of the *apparent* Darcy friction factor, f, given by

$$f = -2D_h \frac{\Delta P/L}{\rho U_b^2}, \tag{1}$$

where U_b is the bulk velocity of the flow in the interior of the microchannel and ρ is the fluid density. This Reynolds-number range is spanned by varying the volumetric flow rate provided by the gear pump and the bulk velocity for each *Re* is therefore evaluated from the known flow rate.

Based on the aforementioned uncertainties in measured quantities, the uncertainty in f is estimated to be 4%.

Since the pressure drop across the microchannel is calculated from measurements of the inlet and outlet pressures, it embodies both the frictional pressure drop across the channel and the incremental pressure defect in the hydrodynamic entrance region of the flow. Therefore, the apparent friction factor, f, calculated using Eq. 1 includes contributions from the hydrodynamically-developing and -developed portions of the flow at a given Re. For laminar flow, Shah and London (1978) found that this apparent friction factor in a smooth rectangular channel can be expressed as

$$f = \frac{K(\infty)}{L/D_h} + f_{fd}, \tag{2}$$

where

$$K(\infty) = 1.20 + \frac{38}{Re} \tag{3}$$

embodies the incremental pressure defect for the entrance of the flow while f_{fd} represents the fully developed friction factor for laminar flow through a rectangular channel of aspect ratio, $\alpha = $ depth/width, given by

$$f_{fd} = \frac{96}{Re}(1 - 1.3553\alpha + 1.9467\alpha^2 - 1.7012\alpha^3 + 0.9564\alpha^4 - 0.2537\alpha^5). \tag{4}$$

This empirical relationship garnered from the numerical studies of Shah and London (1978) therefore provides a basis for comparison of the present apparent friction-factor measurements for both smooth- and rough-wall flows in the laminar regime.

Figure 3 shows f versus Re for all three surface conditions along with f predicted from Eqs. 2 to 4 for the laminar regime using $\alpha = 0.5$ (the aspect ratio of the current microchannel). The present smooth-wall results agree extremely well with the laminar relationship for apparent friction factor in the range $100 \leq Re \leq 1,800$. For reference, we define the highest Re for which laminar flow is apparent (i.e., agreement with laminar flow theory) as the critical Re (Re_{cr}). As such, $Re_{cr} = 1,800$ for the present smooth-wall case. A slight deviation from the laminar flow prediction is first noted at $Re = 1,900$, which is indicative of the onset of transition to turbulence for the smooth-wall case. This observation is quite consistent with that often observed for the onset of transition for flow through macroscale channels (Jones 1976; Obot 1988) as well as recent measurements in circular capillaries (Sharp and Adrian 2004; Natrajan and Christensen 2007, 2009a). Excellent agreement is also noted for flow through both rough-wall microchannels in the lower-Re laminar regime. However, departure from the laminar prediction and the smooth-wall results is observed at lower Re for the two rough-wall

cases. In particular, the inset to Fig. 3 indicates $Re_{cr} = 1,500$ for the R1 case ($k_{rms} = 7.51 \mu m$) and $Re_{cr} = 1,300$ for the R2 case ($k_{rms} = 15.1 \mu m$). Therefore, the present roughness is found to initiate an early departure of the flow from a laminar state, compared to the smooth-wall case, with increasing surface roughness hastening this departure from smooth-wall behavior. While at first glance this roughness-induced deviation from laminar behavior at lower Re might appear unexpected since the seminal roughness experiments of Nikuradse (1933) along with Colebrook and White (1937) and Colebrook (1939) in circular pipes [the latter of which form the basis for the well-known Moody diagram (Moody 1944)] reveal no such dependence of Re_{cr} on ϵ/D_h, evidence of such behavior for flow through passages of non-circular cross-section exists at both the macroscale (Idelchick 1986) and the microscale (Kandlikar et al. 2005; Hao et al. 2006; Liu et al. 2007). However, it should be noted that the observed early departure from laminar behavior in rough-wall microchannels by both Kandlikar et al. (2005) and Hao et al. (2006) occurred at much lower Re ($<1,000$) than that reported herein and in the presence of relatively large and isolated roughness elements [relative roughness of 6–14% for Kandlikar et al. (2005) and 26–32% for Hao et al. (2006)]. On the other hand, the early transition observations of Liu et al. (2007) at $Re \sim 1,100-1,500$ for flow in industrial steel microtubes (2.7–3.5% relative roughness and surface topographies that are more akin to the irregular roughness studied herein) are more consistent with the present observations of roughness-induced transition. Therefore, early departure from laminar, smooth-wall friction-factor trends cannot be fully attributed to unique flow behavior at the microscale but, as argued in Morini (2004), is more likely due to the combined impact of roughness and a non-circular cross-section of the flow passage under consideration.

Upon departing from the laminar prediction, the friction factor increases rapidly with increasing Re until it attains a local maximum in f, following which a turbulent state is eventually attained. Flow for the R2 case approaches a local maximum in f first near $Re = 2,300$, followed by the R1 case ($Re = 2,500$) and then the smooth case ($Re = 2,800$). Interestingly, if one subtracts Re_{cr} for each case from these Re values, one finds the Re-range of the segment of the transitional regime where f increases with Re to be approximately 1,000 for all cases, indicating the bulk transitional pathway for flow in the presence of all three surface cases to be quite similar. Despite this qualitative consistency with respect to Re_{cr}, f is significantly enhanced by roughness, as the maximum values for the R1 and R2 cases are 1.2 and 1.5 times larger, respectively, than that of the smooth-wall case. With further increase in Re, the smooth-wall f again decreases, consistent with

macroscale behavior, while the friction factors for both rough-wall cases asymptote toward constant (but different) values. This tendency toward constant values of f, and therefore independence with increasing Re, in the rough-wall cases represents an approach toward a fully rough state which implies a dominance of form drag over viscous drag with increasing Re (Schlichting 1979). Finally, it is worth noting that these transitional and turbulent friction-factor trends for both the smooth and rough cases are quite consistent with the seminal observations of Nikuradse (1933) and Colebrook (Colebrook and White 1937; Colebrook 1939) for flow through circular pipes as well as the limited data presented in Idelchick (1986) for flow through smooth and rough macroscale ducts of rectangular cross-section.

4.2 Micro-PIV measurements of transitional and turbulent flow

As described in Sect. 2, ensembles of instantaneous velocity fields are acquired by micro-PIV for flow through the rectangular microchannel with three different surface conditions (smooth, R1, and R2) at five different Re: Re_{cr}, $Re_{cr} + 400$, $Re_{cr} + 600$, $Re_{cr} + 1,000$, and $Re_{cr} + 1,600$. Based on the analysis of Natrajan and Christensen (2007) for flow through a circular capillary, the flow should be in its (approximately) early, middle, and latter stages of transition at $Re_{cr} + 400$, $Re_{cr} + 600$, and $Re_{cr} + 1,000$, respectively, and should reach a turbulent state near $Re_{cr} + 1,600$. As described below, these approximate classifications also hold for both the present smooth-wall rectangular microchannel case as well as the R1 and R2 cases. Therefore, these micro-PIV measurements span the entire Re-range over which the flow transitions from a laminar to a fully turbulent state for all three surface conditions. Table 2 summarizes the relevant parameters of these experiments.
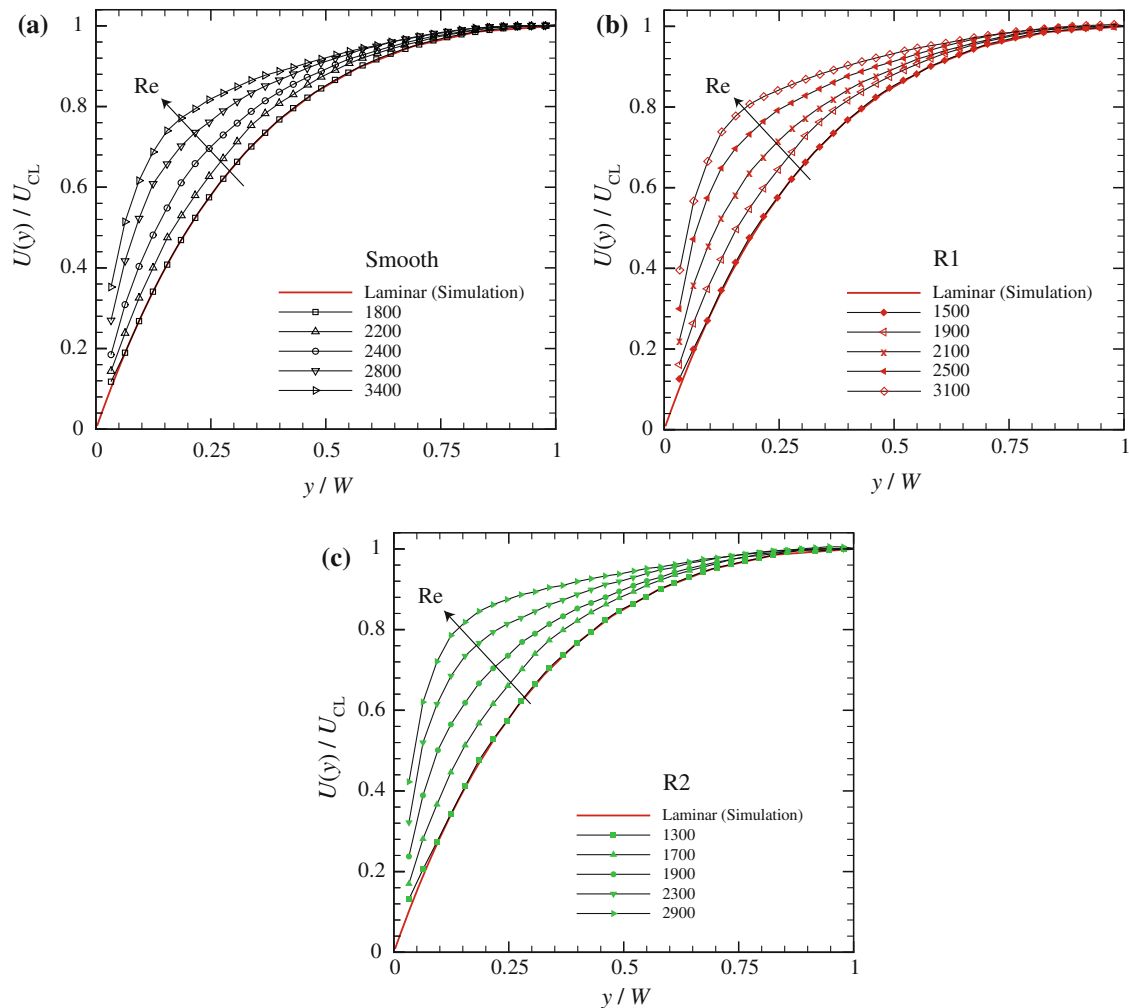
4.2.1 Mean velocity profiles

Figure 4a–c shows the mean velocity profiles, $U(y)/U_{CL}$ (where U_{CL} is the centerline velocity), as a function of the wall-normal position, y/W, in the range $Re_{cr} \leq Re \leq Re_{cr} + 1,600$, for the smooth, R1 and R2 cases, respectively. These profiles are computed by ensemble averaging all of the instantaneous realizations acquired by micro-PIV at each Re for the smooth- and rough-wall cases followed by line averaging in the streamwise direction. For comparison, the mean velocity profile for fully developed laminar flow, U_{lam}, obtained via a numerical simulation of the flow through the full geometry of the present microchannel using the *Fluent* software package is included in Fig. 4a–c. In order to replicate the current flow conditions, these simulations are performed over a computational

Table 2 Summary of micro-PIV experimental parameters

Surface condition	Re	U_b (m/s)	No. of realizations
Smooth	1,800	2.99	834
	2,200	3.66	822
	2,400	3.99	852
	2,800	4.66	826
	3,400	5.66	817
R1	1,500	2.49	828
	1,900	3.16	815
	2,100	3.49	809
	2,500	4.16	845
	3,100	5.16	833
R2	1,300	2.16	839
	1,700	2.83	827
	1,900	3.16	832
	2,300	3.83	815
	2,900	4.83	828

The vector grid spacings in the streamwise and wall-normal directions for all the data sets are $\Delta x = \Delta y = 11.9\,\mu m$

domain of $900\,\mu m \times 450\,\mu m \times 306\,mm$ that is discretized using a $48 \times 24 \times 306$ (y–z–x) grid with a symmetry boundary condition specified at the midplane of the flow domain in order to reduce the grid size. A uniform velocity profile is specified at the inlet of the test section while an atmospheric pressure outflow boundary condition is specified at the exit to replicate the experimental conditions. Finally, a grid-independence test was performed to ensure that the computational grid employed herein was sufficient to capture the relevant physics. For the smooth-wall case (Fig. 4a), at $Re = 1,800$, the mean velocity profile reveals a parabolic trend that is in excellent agreement with the mean profile for fully developed laminar flow obtained from the numerical simulations. This inference of laminar flow at $Re = 1,800$ is consistent with both the friction-factor behavior in Fig. 3, where the smooth-wall f agrees with the laminar prediction of Shah and London (1978) at this Re as well as smooth-wall circular capillary flow measurements, where the mean velocity profiles for $Re \leq 1,800$ collapsed with the analytical profile for fully developed laminar flow (Natrajan and Christensen 2007). With increasing Re, the smooth-wall mean velocity profiles deviate from this laminar behavior and become progressively flatter and fuller in character. Again, these trends are consistent both with the friction-factor trends at these Re for smooth-wall flow which reveal departure from laminar behavior as it transitions toward a turbulent state and with the mean velocity profiles of Natrajan and Christensen (2007) in circular capillaries that suggest the flow to be in
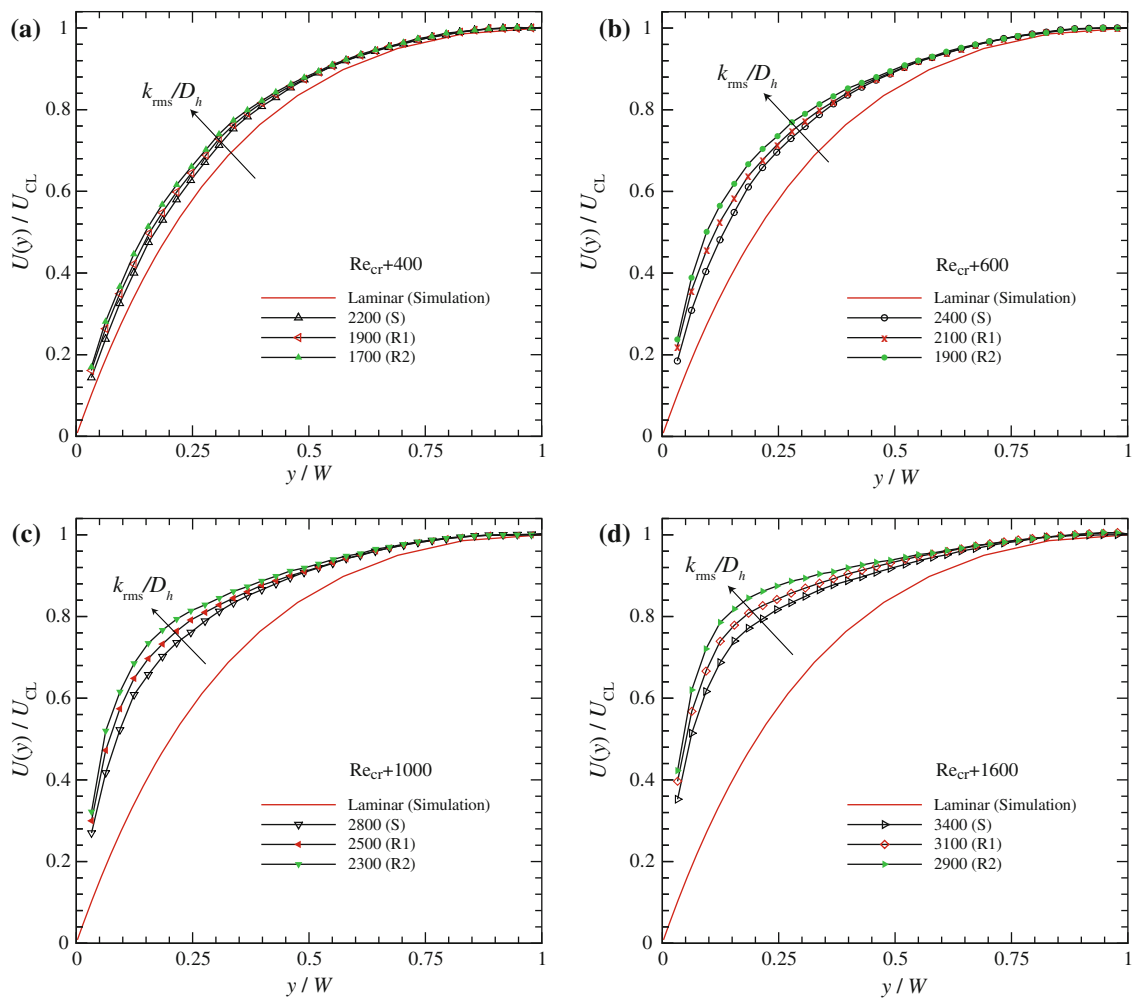
Fig. 4 Mean velocity profiles as a function of wall-normal position, *y/W*, for flow through the copper microchannel fitted with the **a** smooth, **b** R1, and **c** R2 side-wall inserts

its early, midway, and latter stages of transition at $Re = 2,200$, 2,400, and 2,800, respectively, with a fully turbulent state attained near $Re = 3,400$.

Similar Reynolds-number trends in the mean velocity profiles are noted for flow in the presence of roughness (Fig. 4b, c for the R1 and R2 surfaces, respectively). In particular, while excellent agreement is observed between the mean velocity profiles at $Re = 1,500$ and $Re = 1,300$ (Re_{cr} for the R1 and R2 cases, respectively) and the numerical prediction for fully developed laminar flow, deviation from laminar behavior is noted for $Re > Re_{cr}$ for both rough surfaces. Consistent with the smooth-wall trends, the rough-wall mean velocity profiles become progressively flatter and fuller as the flow transitions from a laminar to a turbulent state. These observations are again in accordance with the friction-factor trends for these surfaces where collapse with the laminar prediction of Shah and London (1978) is observed at Re_{cr}, while deviation

from the laminar prediction is noted for $Re > Re_{cr}$ where the friction factor increases as the flow approaches a turbulent state. Therefore, these rough-wall mean velocity profiles support a relatively gradual progression in the transition of the flow from a laminar to a turbulent state much like that for smooth-wall flow with the onset of transition occurring at $Re > Re_{cr}$, where Re_{cr} decreases with increasing degree of surface roughness. Finally, the profiles shown in Fig. 4 indicate that deviation of the mean velocity profile from the laminar profile increases with increasing surface roughness at fixed Re in the transitional regime. For instance, while a slight deviation from the laminar profile is noted for the R1 case at $Re = 1,900$ (Fig. 4b), the mean velocity profile at this Re is comparatively flatter and fuller for the R2 case (Fig. 4c). These differences imply that the flow at this Re for the R2 case is further along in the transition process than flow at this Re for the R1 case which is consistent with the fact that

Fig. 5 Comparison of the mean velocity profiles, as a function of the wall-normal position, y/W, for flow through the copper microchannel fitted with the smooth, R1 and R2 side-wall inserts at **a** $Re_{cr} + 400$, **b** $Re_{cr} + 600$, **c** $Re_{cr} + 1,000$ and **d** $Re_{cr} + 1,600$

$Re_{cr}^{R2} < Re_{cr}^{R1}$. As such, these trends further support the inference from the friction-factor trends that the hastening of the flow toward a turbulent state increases with increasing degree of surface roughness.

The mean velocity profiles for different surface conditions can be further contrasted by directly comparing them relative to the onset of transition rather than at absolute Re since it is clear that Re_{cr} is a function of roughness. Figure 5a–d shows the profiles of mean velocity at $Re_{cr} + 400$, $Re_{cr} + 600$, $Re_{cr} + 1,000$, and $Re_{cr} + 1,600$, respectively, for the smooth, R1 and R2 cases. At $Re_{cr} + 400$ (Fig. 5a), while the mean velocity profiles for all three surface conditions collapse well in the region close to the centerline of the microchannel $(0.5 \lesssim y/W \leq 1)$, slight differences are apparent in the region closer to the wall $(y/W \lesssim 0.5)$. In particular, the velocity profiles are flatter and fuller with increasing surface roughness, resulting in larger velocity gradients in the region close to the wall which account for increased values of wall shear stress and

hence friction factor with increasing roughness. Similar trends are also apparent for transitional flow at $Re_{cr} + 600$ and $Re_{cr} + 1,000$ (Fig. 4b, c, respectively), for which the differences in the mean velocity profiles in the region $y/W \lesssim 0.5$ with increasing roughness become more pronounced as the flow tends toward a turbulent state. Finally, at $Re_{cr} + 1,600$ (Fig. 5d), where the flow for the smooth-wall case is close to a fully turbulent state based on the previous observations of Natrajan and Christensen (2007), the roughness profiles appear significantly flatter and fuller than their smooth-wall counterpart with this deviation more stark with increasing roughness. These trends, particularly the observations of larger velocity gradients in the near-wall region which results in an enhancement of drag at the surface with increasing roughness, are entirely consistent with the friction-factor trends in Fig. 3, where f is found to increase significantly with increasing surface roughness. These differences are particularly notable in the latter stages of the transition process.

4.2.2 Laminar and non-laminar subsets

The progression of the mean velocity profiles in Fig. 4 toward a flatter and fuller state with increasing Re can be interpreted in terms of the aforementioned observations of more frequent occurrences of turbulent spots at transitional Re amidst less frequent observations of nominally laminar flow as is well-established at the macroscale and now at the microscale (Natrajan and Christensen 2007). In this context, the fuller character of the rough-wall profiles in Fig. 5 compared to smooth-wall flow at fixed Re relative to Re_{cr} may be attributable to the increasingly frequent occurrence of and/or the existence of more-intense turbulent spots at a given Re relative to Re_{cr} with increasing roughness. In order to investigate these possibilities, the instantaneous velocity fields at each Re that embody disordered (non-laminar) behavior for all three surface conditions must first be identified from those fields capturing laminar behavior. This distinction in transitional smooth-wall capillary flow is achieved by comparing the instantaneous streamwise velocity profile at each streamwise location, x, in an instantaneous velocity field to the expected laminar velocity profile for fully developed flow as a means of identifying fields embodying laminar and non-laminar behavior (recall that all measurements occur sufficiently downstream of the entrance region so that fully developed flow is ensured) (Natrajan and Christensen 2007). For the present ensembles of instantaneous velocity fields, the instantaneous streamwise velocity profile at a given x in a realization is first normalized by its instantaneous centerline velocity to yield an instantaneous streamwise velocity profile that varies from zero at the walls to a value of one at the centerline. Following this, the deviation, ς, of an instantaneous streamwise velocity profile at a given streamwise location from the fully developed laminar velocity profile is quantified as

$$\varsigma(x; Re; \epsilon/D_h) = \frac{1}{2W} \int_0^{2W} \left| \frac{u(y; x; Re; \epsilon/D_h) - U_{lam(y)}}{u(y; x; Re; \epsilon/D_h)} \right| dy,$$
(5)

where $U_{lam}(y)$ is the fully developed laminar velocity profile obtained from the aforementioned numerical simulations. Therefore, ς provides a measure of the deviation of an instantaneous streamwise velocity profile at a given streamwise location from the fully developed laminar velocity profile and will only be non-zero for velocity profiles that exhibit a departure from laminar behavior. As such, computation of ς for the instantaneous velocity profiles at all streamwise locations within every statistically independent velocity realization at a given Re and surface condition provides a means of separating laminar and non-laminar profiles in the velocity ensembles.

However, to account for finite errors associated with the measurement of instantaneous velocities using micro-PIV, a threshold of $\varsigma \leq 0.05$ (5% deviation) is employed (see Natrajan and Christensen 2007). Using this methodology, one can determine the fraction of the instantaneous streamwise velocity profiles at a given Re and surface condition that exhibit laminar behavior as

$$\chi(Re, \epsilon/D_h) = \frac{1}{NM} \sum_{j=1}^{NM} I_\varsigma(x_j; Re; \epsilon/D_h),$$
(6)

where N and M are the number of realizations and streamwise measurement positions per realization, respectively, and the indicator function, I_ς, is given by

$$I_\varsigma(x_j; Re; \epsilon/D_h) = \begin{cases} 1 & \text{when } \varsigma(x_j; Re; \epsilon/D_h) \leq 0.05 \\ 0 & \text{otherwise.} \end{cases}$$
(7)

Note that $1 - \chi$ equivalently gives the fraction of non-laminar profiles at a given Re and surface condition.

Figure 6a shows the variation of the laminar (χ) and the non-laminar ($1 - \chi$) fractions as a function of Re for all three surface conditions. For comparison, the Reynolds-number variations of χ and $1 - \chi$ for smooth-wall capillary flow (Natrajan and Christensen 2007) are also presented in Fig. 6a. For the present smooth-wall case, the values of the laminar fraction $\chi = 1$ and 0 at $Re = 1,800$ and 3,400, respectively, are entirely consistent with observations of laminar and turbulent flow at these Re as interpreted from the mean velocity profiles in Fig. 4a as well as the friction-factor trends in Fig. 3. Further, these upper and lower limits on laminar and turbulent flow, respectively, agree well with those observed for smooth-wall capillary flow (Natrajan and Christensen 2007). In addition, the values of $\chi \approx 0.78$, 0.49, and 0.19, at $Re = 2,200$, 2,400, and 2,800, respectively, for the present rectangular cross-section smooth-wall flow are consistent the values of χ for smooth-wall capillary flow and suggest the flow at these Re to be in the early, middle, and latter stages of transition, respectively. This consistency between the laminar and non-laminar fractions for flow in rectangular and circular cross-section passages also suggests that the cross-sectional geometry has little impact on the occurrence of turbulent spots at fixed Re in smooth-wall flow. Turning to the rough-wall trends, the R1 and R2 cases achieve values of $\chi = 1$ at $Re = 1,500$ and 1,300, respectively, indicating that all streamwise velocity profiles exhibit fully developed laminar behavior at these Re. This behavior is in accordance with the collapse of the mean velocity profiles with the numerical prediction for laminar flow at these Re in Fig. 4 and the observations of laminar flow for $Re_{cr} \leq 1,500$ and 1,300 for the R1 and R2 cases, respectively, based on friction-factor measurements. Consistent with the smooth-wall trends, the laminar fraction progressively
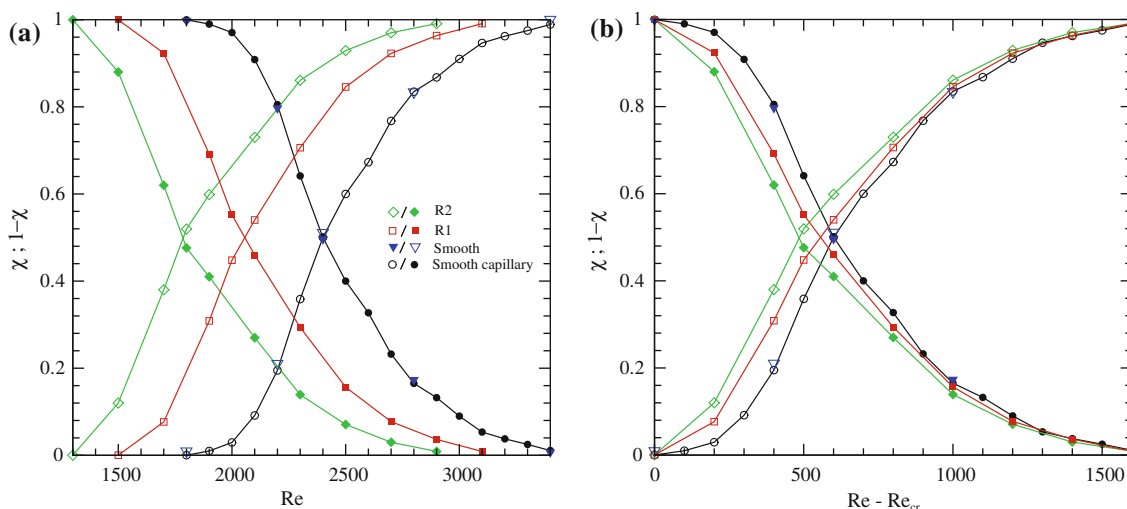
Fig. 6 Variation of laminar (χ; *filled symbols*) and non-laminar ($1 - \chi$; *hollow symbols*) fractions for the smooth- and rough-wall cases as a function of **a** Re and **b** $Re - Re_{cr}$

decreases with increasing Re for both the R1 and R2 cases until a value of $\chi = 0$ is attained at $Re = 3{,}100$ and $2{,}900$, respectively. Further, consistent with the mean velocity profiles (Fig. 4), the trends of χ and $1 - \chi$ in Fig. 6a support the inference of a hastening of the flow toward a turbulent state with increasing surface roughness due to the initiation of transition at lower critical Re. For instance, at $Re = 2{,}100$ the flow for the smooth, R1 and R2 cases is found to be in the early, middle, and latter stages of transition, respectively, based on laminar fractions of 0.2, 0.68, and 0.86.

Interestingly, the χ and $1 - \chi$ curves for the R1 and R2 cases in Fig. 6a appear quite similar to their smooth-wall counterparts save for a shift in Re_{cr} toward lower values with increasing roughness. This consistency is directly assessed in Fig. 6b where the χ and $1 - \chi$ curves are plotted as a function of $Re - Re_{cr}$ for the smooth, R1 and R2 cases. Such a comparison allows one to investigate the similarities and differences in the transitional pathway of the flow as it transitions from a laminar to turbulent state for the smooth- and the rough-wall cases relative to Re_{cr} at which transition is first initiated. As expected from the friction-factor and mean-velocity-profile trends, $\chi = 1$ at $Re - Re_{cr} = 0$ for all three surfaces. However, a clear enhancement in the growth rate of the fraction of the flow that exhibits non-laminar behavior with increasing surface roughness is observed for $Re > Re_{cr}$ as $(1 - \chi)_{SM} < (1 - \chi)_{R1} < (1 - \chi)_{R2}$. Interestingly, this enhancement in the growth rate of the non-laminar fraction with increasing surface roughness is most pronounced when the flow is in the early stages of transition. With further increase in Re relative to Re_{cr}, the differences in $1 - \chi$ for the three surface conditions steadily decrease until $1 - \chi$ reaches unity for all surfaces at $Re = Re_{cr} + 1{,}600$. For instance, at

$Re = Re_{cr} + 400$ (when the flow is in the early stages of transition) the smooth, R1 and R2 cases have $1 - \chi$ values of roughly 0.2, 0.29, and 0.39, respectively, while at $Re = Re_{cr} + 600$ (when the flow is roughly midway between the laminar and turbulent states) $1 - \chi \approx 0.51$, 0.55, and 0.59, respectively. In contrast, at $Re = Re_{cr} + 1{,}000$ (when the flow in its latter stages of transition) the values of $1 - \chi$ are roughly 0.81, 0.82, and 0.83 for the smooth, R1 and R2 cases, respectively. Therefore, an accelerated pathway toward a turbulent state exists with an increasing number of velocity fields embodying disordered motion with increasing roughness in the early stages of transition. However, this effect of roughness diminishes as a turbulent state is approached in such a way that the Reynolds-number span of the transitional regime is essentially the same for all three surface conditions. One possible explanation for the enhanced growth of disordered motion in the early stages of transition lies in the likely generation of more energetic disturbances with increasing degree of surface roughness that can more easily overcome the damping effect of viscosity at fixed Re compared to smooth-wall conditions. Under such a scenario, the probability of disturbances growing into turbulent spots at fixed Re is likely higher with increasing surface roughness due to this enhanced disturbance energy.

4.2.3 Instantaneous structure

Figure 7a–c shows Galilean-decomposed representative non-laminar instantaneous velocity fields in the streamwise–wall-normal plane of the rectangular microchannel at $Re_{cr} + 600$ at which the flow is roughly midway between a laminar and turbulent state with non-laminar fractions ($1 - \chi$) of 0.51, 0.55, and 0.59 for the smooth, R1 and R2
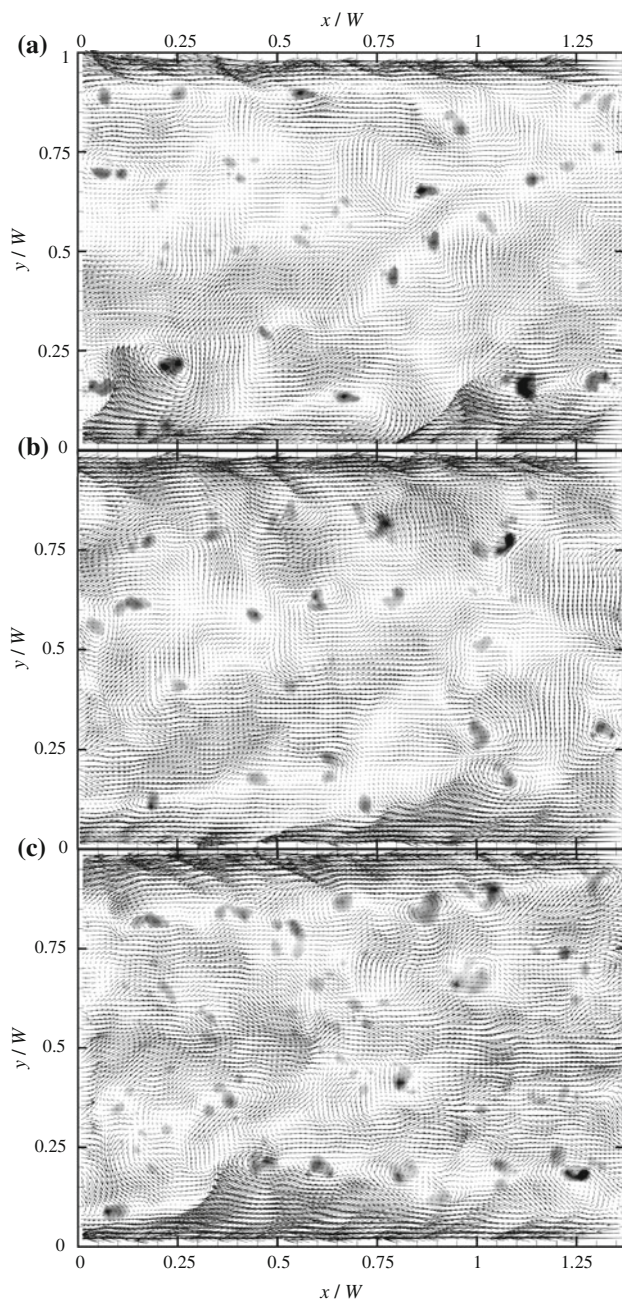
Fig. 7 Galilean-decomposed instantaneous velocity fields in the $x-y$ plane at $Re_{cr} + 600$ for transitional flow through the copper micro-channel fitted with the **a** smooth ($U_c = 0.80U_{CL}$), **b** R1 ($U_c = 0.78U_{CL}$), and **c** R2 ($U_c = 0.81U_{CL}$) side-wall inserts. Contours of λ_{ci} are presented in the background of all vector fields to highlight vortex cores

cases, respectively. These fields were identified using the methodology described in the previous section. Galilean decomposition is chosen for visualization of these fields since removal of a fixed advection velocity from an instantaneous velocity field reveals vortices traveling at this velocity as closed streamline patterns, consistent with

the definition of a vortex offered by Kline and Robinson (1989). This method is therefore well-suited for visualizing the local flow kinematics induced by these vortices. In addition, a local, Galilean-invariant vortex identifier, swirling strength (λ_{ci}), is employed since one would have to remove a broad range of advection velocities to reveal all embedded structure using Galilean decomposition alone. Swirling strength (λ_{ci}) is the imaginary part of the complex-conjugate eigenvalues of $\nabla \mathbf{u}$ and is an unambiguous identifier of rotation (Zhou et al. 1999; Adrian et al. 2000a). Each of the instantaneous velocity fields in Fig. 7 contains several closed-streamline patterns that represent sections of spanwise vortex cores advecting in the streamwise direction. For comparison, contours of instantaneous λ_{ci} are also shown in the background of each velocity field and all of the closed streamline patterns visualized in the Galilean decompositions are spatially coincident to clusters of non-zero λ_{ci}. In addition, the sense of rotation of these swirling motions, predominantly clockwise and counter-clockwise in the lower and upper halves of the flow, respectively, is consistent with the sense of the mean shear in these regions. Further, several clusters of non-zero λ_{ci} are noted at locations that are devoid of swirling patterns and these additional clusters represent slices through vortices that are not advecting at U_c. Clearly the flow behavior captured in all three representative fields is far from laminar given the extremely active structure noted throughout the smooth- and rough-wall examples.

Turning to the bottom half of the smooth-wall field presented in Fig. 7a, each of the visualized spanwise vortex cores induces a strong ejection of low-speed fluid away from the wall (also referred to as a Q_2 event in the nomenclature of Lu and Willmarth (1973) with $u' < 0$ and $v' > 0$, where u' and v' are the fluctuating streamwise and wall-normal velocities, respectively) just upstream and below of its core (similar characteristics are also apparent for the vortices visualized in the upper half of the flow). These ejection events contribute significantly to the Reynolds shear stress (RSS) contained in the flow field and play a significant role in transport processes within the non-laminar portions of the flow (Natrajan and Christensen 2007, 2009a) including the generation of additional friction at the wall. Further, these spanwise vortices appear to align in the streamwise direction, forming an interface that is slightly inclined away from the wall. A large-scale region of streamwise momentum deficit is noted in the vicinity of the wall beneath this interface which is likely due to the collective induction of the streamwise-aligned vortices. Similar qualitative structural attributes are readily apparent in the non-laminar fields for the R1 and R2 cases (Fig. 7b, c, respectively) and, as noted for smooth-wall transitional capillary flow (Natrajan and Christensen 2007), these spatial signatures are quite consistent with observations of

hairpin vortices and their organization into larger scale hairpin-vortex packets in macroscale studies of both turbulent (Adrian et al. 2000b; Christensen and Adrian 2001; Ganapathisubramani et al. 2003) and transitional wall-bounded flows (Schröder and Kompenhans 2004). As such, the present roughness does not appear to alter the general structural paradigm of the turbulent spots compared to smooth-wall flow. However, quantitative differences are indeed apparent between the smooth- and rough-wall flows. In particular, the intensity of the velocity fluctuations as well as the structural activity at this fixed value of $Re - Re_{cr} = 600$ is clearly enhanced with increasing surface roughness. For example, many more clusters of non-zero λ_{ci} (indicative of spanwise vortex cores) are visualized in the R2 case (Fig. 7c) compared to both the smooth (Fig. 7a) and R1 (Fig. 7b) cases. As a result of this increased structural activity, it is likely that more numerous and/or intense RSS-producing ejections events will be generated with increasing roughness which, in concert with increasing magnitudes of the mean velocity gradients, enhance the production of disordered (turbulent) activity within the non-laminar portions of transitional microchannel flow. For reference, instantaneous non-laminar fields for the smooth, R1 and R2 cases in the transitional regime at other Re (not presented herein for brevity) display similar trends, with the roughness-induced intensification of both the velocity fluctuations and the structural activity becoming progressively pronounced as the flow tends toward a turbulent state.

The enhancement in the structural activity of the non-laminar portions of the flow with increasing roughness, as suggested by the instantaneous fields in Fig. 7, can be quantified by considering RMS profiles of λ_{ci}, σ_λ, as a function of wall-normal position, y/W for the smooth, R1 and R2 cases at various Re relative to Re_{cr} in the transitional regime (Fig. 8). The smooth-wall profiles of σ_λ exhibit clear peaks that both increase in magnitude and shift closer to the wall with increasing Re. These trends are quite consistent with the behavior of smooth-wall capillary flow, further supporting strong structural similarities between transitional flow in circular and non-circular cross-sections at the microscale. Interestingly, the profiles of σ_λ for the R1 and R2 cases exhibit a noted increase in magnitude in the near-wall region ($y/W \lesssim 0.5$) as well as a slight shift in the peak location toward the wall with increasing surface roughness for fixed $Re - Re_{cr}$. Further, the width of the peak in σ_λ broadens with increasing roughness and these differences between the smooth- and rough-wall cases become more pronounced with increasing $Re - Re_{cr}$. In contrast, σ_λ shows little impact of roughness in the core of the flow as all three surface cases collapse and tend toward a constant value as the centerline of the microchannel is approached for fixed $Re - Re_{cr}$. Together
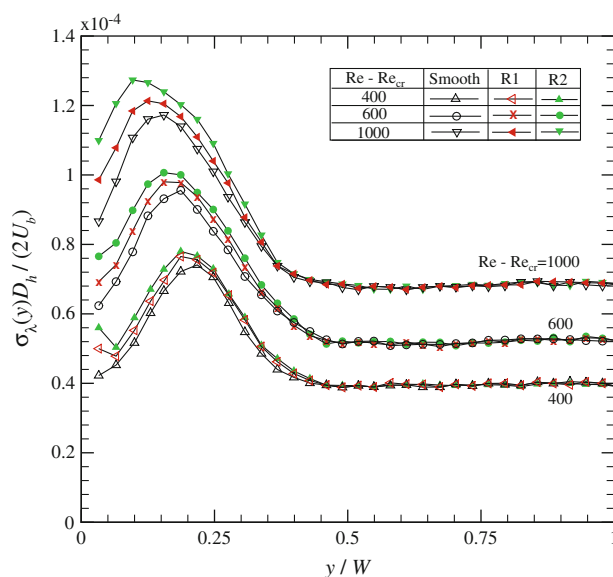

Fig. 8 Root-mean-square profiles of λ_{ci}, σ_λ, as a function of wall-normal position, y/W, at various Re

with the differences noted in the instantaneous velocity fields (Fig. 7), this enhancement of σ_λ with increasing surface roughness can be attributed to an increased population of spanwise vortical structures as well as a possible enhancement in the strength of these vortices due to increased roughness effects. This departure from smooth-wall trends becomes more pronounced as a turbulent state is approached.

4.2.4 Single-point statistics of the non-laminar ensembles

The maturation of the underlying disorder through the transitional regime both with increasing Re and surface roughness can be further quantified through single-point statistics of the non-laminar ensembles. These single-point statistics are computed by ensemble- and line-averaging over the subset of instantaneous velocity profiles embodying non-laminar (disordered) behavior at each Re for each surface condition. Figure 9a shows mean streamwise velocity profiles of the non-laminar ensembles for each surface condition, $U_{nl}(y)$, normalized by the corresponding mean centerline velocity. Only the profiles at $Re_{cr} + 400$ and $Re_{cr} + 1,000$, where the flow is in the early and latter stages of transition, respectively, are presented for clarity. For comparison, the aforementioned fully developed laminar profile from numerical simulation is included as well. Consistent with that noted for smooth-wall capillary flow (Natrajan and Christensen 2007), the Reynolds-number trends of the mean profiles computed from the non-laminar ensembles for fixed surface condition suggest a continual maturation of the non-laminar portions of the flow until a fully turbulent state is attained. Of particular interest, the
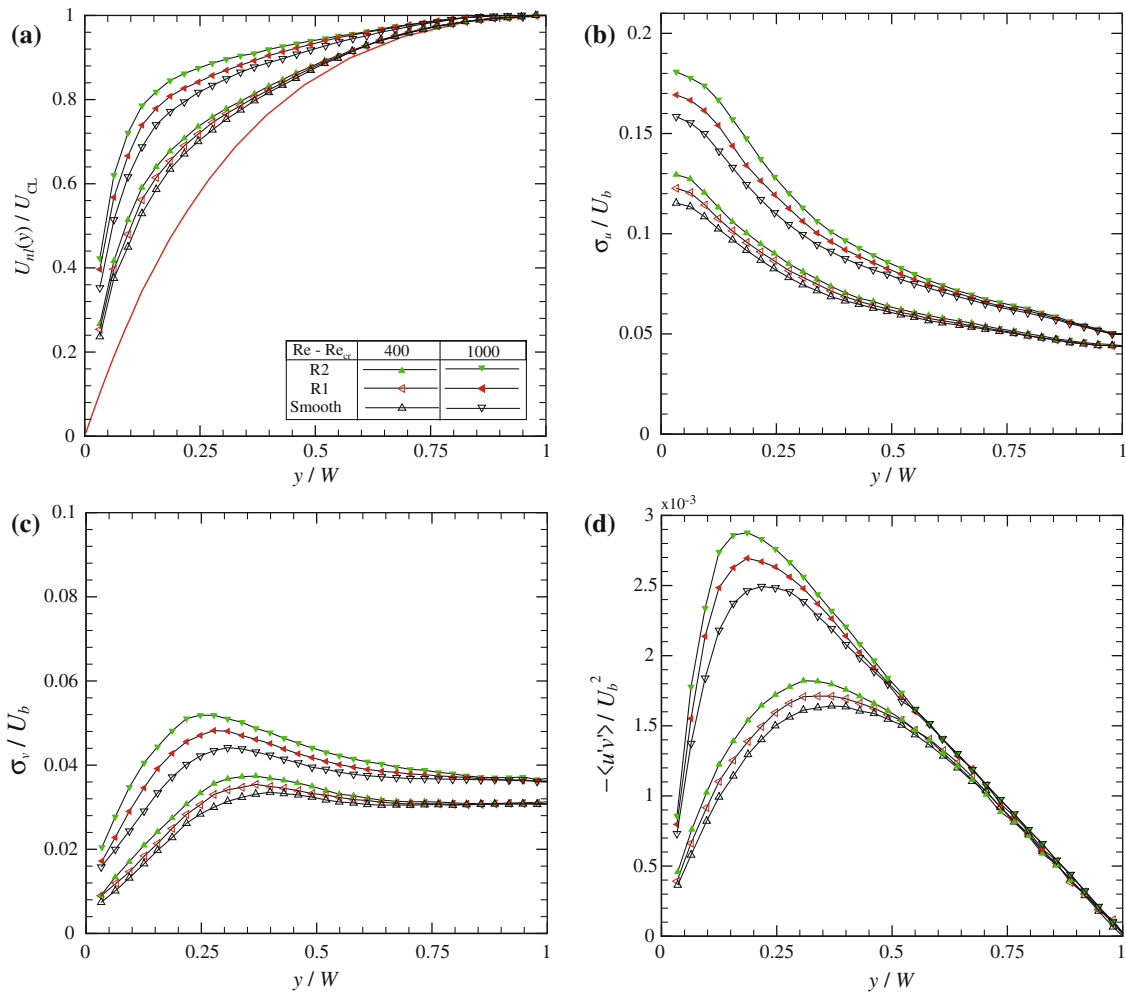
Fig. 9 Single-point statistics for the non-laminar ensembles at $Re_{cr} + 400$ and $Re_{cr} + 1,000$ for the smooth- and rough-wall cases. **a** Mean velocity profiles of the non-laminar ensembles, $U_{nl}(y)$, normalized by mean centerline velocity, U_{cl}; **b**, **c** profiles of streamwise and wall-

mean non-laminar streamwise velocity profiles for the smooth, R1 and R2 cases do not collapse at fixed $Re - Re_{cr}$, but rather become considerably flatter and fuller with increasing surface roughness. These differences become more pronounced as the flow approaches a turbulent state. This flattening, which yields a more intense velocity gradient at the wall with increasing surface roughness, is consistent with the enhancement of friction factor noted throughout the transitional and turbulent regimes with increasing roughness.

The single-point statistics of the velocity fluctuations of the non-laminar ensembles are also assessed by decomposing each of the instantaneous velocity profiles in a given non-laminar ensemble as

$$u_i(x, y, z, t) = U_i(y) + u_i'(x, y, z, t), \quad (8)$$

where $u_i = (u, v)$ is the instantaneous non-laminar velocity, $U_i = (U_{nl}, 0)$ is the mean non-laminar velocity profile for a

normal RMS velocities, σ_u and σ_v, respectively, normalized by bulk velocity, U_b; **d** Reynolds shear stress profiles, $-\langle u'v' \rangle$, normalized by U_b^2

given Re (presented in Fig. 9a), and $u_i' = (u', v')$ represents the instantaneous non-laminar streamwise and wall-normal velocity fluctuations. Using the resulting ensembles of instantaneous, non-laminar fluctuating velocity fields, the RMS of the non-laminar streamwise and wall-normal velocities, σ_u and σ_v, respectively, and the Reynolds shear stress, $-\langle u'v' \rangle$, are computed using the same streamwise-averaging procedure described above. Figure 9b, c shows σ_u and σ_v computed from the non-laminar ensembles normalized by the bulk velocity, U_b, respectively, for the smooth, R1 and R2 cases at $Re_{cr} + 400$ and $Re_{cr} + 1,000$. At fixed $Re - Re_{cr}$, the smooth- and rough-wall profiles of σ_u and σ_v collapse near the centerline of the microchannel ($y/W \gtrsim 0.75$), consistent with the profiles of RMS swirling strength. As the wall is approached, however, differences between the smooth- and rough-wall profiles of σ_u and σ_v become increasingly apparent. In particular, a progressive increase in σ_u and σ_v is noted with increasing surface

roughness and decreasing distance from the wall as well as a clear shift in the peak location of these quantities toward the wall with increasing roughness. These differences become more pronounced with increasing Re as the flow approaches a turbulent state, consistent with that observed in profiles of the mean streamwise velocity for the non-laminar ensembles (Fig. 9a).

Finally, Fig. 9d presents profiles of the Reynolds shear stress, $-\langle u'v' \rangle$, for the smooth and the rough-wall cases at $Re_{cr} + 400$ and $Re_{cr} + 1,000$. Interestingly, at fixed $Re - Re_{cr}$, excellent collapse of the RSS profiles for the smooth, R1 and R2 cases is noted in the core of the flow ($y/W \gtrsim 0.5$) where the profiles exhibit a linear region from the centerline to the peak location. This linear behavior is characteristic of transitional and turbulent wall-bounded flows and represents a dominance of turbulent (inertial) effects over viscous stresses. As the wall is approached for fixed $Re - Re_{cr}$, deviation from the smooth-wall mean RSS profile is noted for the rough-wall cases as the magnitude of the peak in the RSS increases with increasing surface roughness coupled with a shift in the peak location closer to the wall. As with σ_u and σ_v, the increase in the peak magnitudes of $-\langle u'v' \rangle$ with increasing surface roughness is more pronounced in the latter stages of transition as the flow approaches a turbulent state. Taken together with the qualitative observations of more vigourous disordered motions at fixed $Re - Re_{cr}$ with increasing roughness in the instantaneous fields of Fig. 7, the growth of σ_u, σ_v and $-\langle u'v' \rangle$ at fixed $Re - Re_{cr}$ with increasing surface roughness supports an amplification of the velocity fluctuations by surface roughness that becomes increasingly apparent at higher Re in the transitional regime.
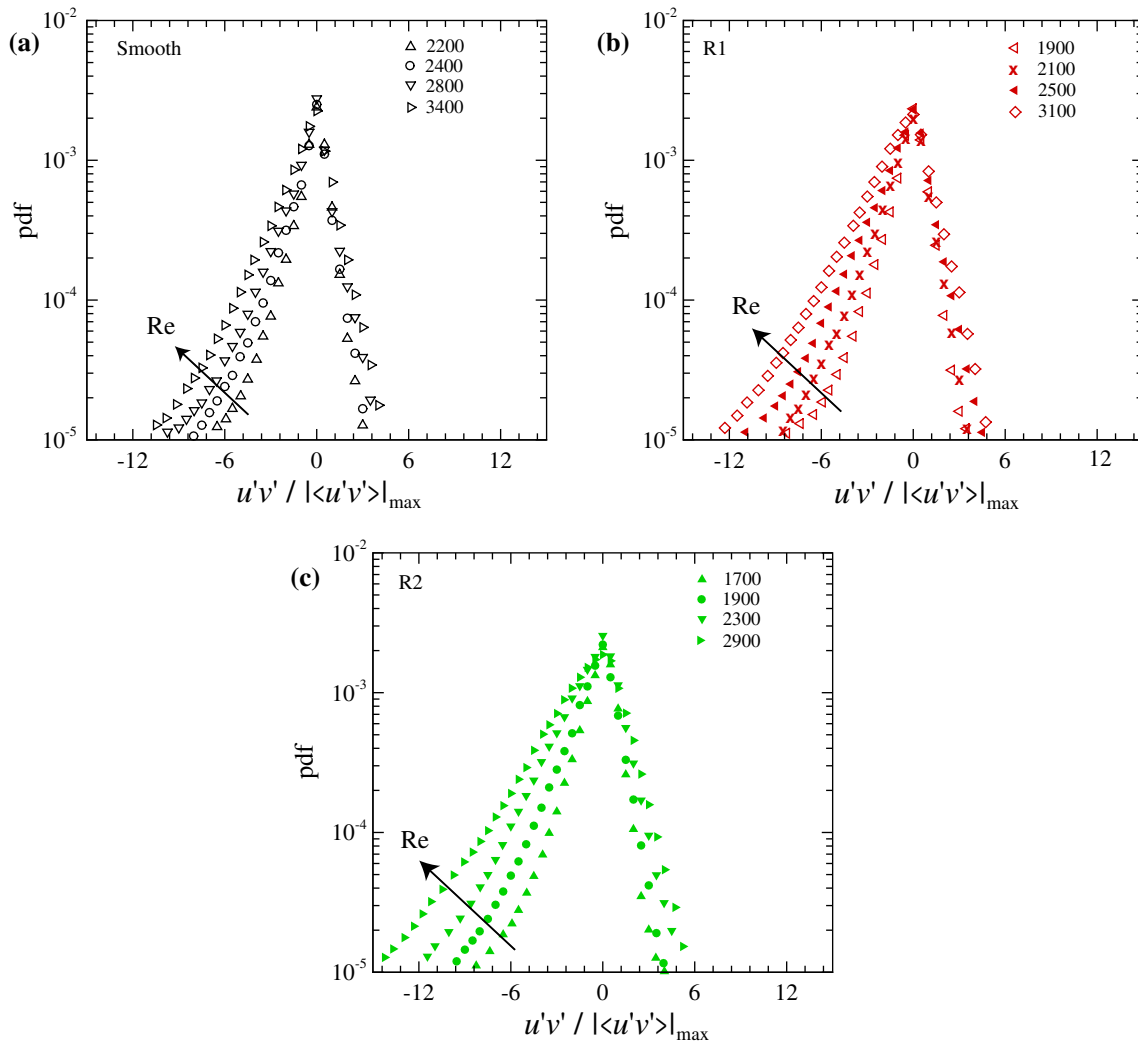
4.2.5 Probability density functions of $u'v'$

The coupled growth of the mean streamwise velocity gradient, $\partial U / \partial y$, and the mean RSS, $\langle u'v' \rangle$, with increasing roughness is of particular interest because the product of these quantities occurs in the kinetic energy equation for the disturbances (equivalently the turbulent kinetic energy equation for fully turbulent flow) and represents either a source or sink of disturbance (turbulent) kinetic energy depending upon their signs. For the present case, $\partial U / \partial y > 0$ and $\langle u'v' \rangle < 0$ throughout the flow, meaning their product acts as a *source* of disturbance kinetic energy in the transitional regime and eventually turbulent kinetic energy upon attainment of a turbulent state by drawing energy from the mean (base) flow. Therefore, it is of interest to explore how the mean RSS is enhanced in the presence of surface roughness. In particular, the mean RSS is constructed from the instantaneous $u'v'$ events that occur within the flow and these contributions can be subdivided into four different types of events depending upon the sign

of the velocity fluctuations. In the nomenclature of Lu and Willmarth (1973), instantaneous $u'v'$ events can be classified based upon the quadrant (Q_i) in the $u'-v'$ plane in which it resides: outward interactions (Q_1; $u' > 0$ and $v' > 0$), ejections (Q_2; $u' < 0$ and $v' > 0$), inward interactions (Q_3; $u' < 0$ and $v' < 0$) and sweeps (Q_4; $u' > 0$ and $v' < 0$). Since the mean RSS is negative, one can ascertain that ejections and/or sweeps dominate over inward and outward interactions in a mean sense. However, it is of interest to uncover how the balances between these different contributions in smooth-wall flow might be altered and/or enhanced by surface roughness through the transitional and turbulent regimes.

Figure 10a–c shows probability density functions (pdfs) of instantaneous $u'v'$ events at $y = 0.25W$ for the smooth, R1 and R2 cases, respectively, normalized by the absolute value of the peak RSS at each Re and surface condition. This wall-normal location is selected for analysis because it resides near the peak mean RSS for all surface conditions and Re. The pdfs computed at all Re for the three surface conditions are notably skewed toward negative values, which is consistent with the sign of the mean RSS profiles in Fig. 9d and the observations of Natrajan and Christensen (2009a) for smooth-wall capillary flow. In the context of quadrant events, this skew toward negative $u'v'$ values confirms the dominance of ejection/sweep events over inward/outward interactions. Interestingly, while the vast majority of the RSS-producing events are quite small in magnitude irrespective of surface condition, there exist a small number of extremely intense instantaneous $u'v'$ (6–12 times larger than the peak mean RSS) that contribute to the mean RSS in both the transitional and turbulent flow cases. With regard to smooth-wall flow, Fig. 10a reveals a progressive increase in the number of negative $u'v'$ events with increasing Re particularly for the most intense negative $u'v'$ events. On the other hand, the number of positive $u'v'$ events increases only slightly with increase in Re. Interestingly, the relative enhancement in the magnitudes of the negative $u'v'$ events with increasing Re for the R1 case (Fig. 10b) is more pronounced than that noted for the smooth-wall case though little difference between the smooth and R1 cases is apparent in the positive $u'v'$ tails. Similarly, the negative tails of the pdfs for the R2 case (Fig. 10c) grow even more substantially with increasing Re compared to both the R1 and smooth cases suggesting a progressive enhancement of ejection/sweep events with increasing surface roughness. While much weaker, a slight enhancement in positive $u'v'$ events is also noted for the R2 case with increasing Re.

In order to further explore the impact of surface roughness on the instantaneous $u'v'$ events contributing to the mean RSS, Fig. 11a–d shows direct comparisons of $u'v'$ pdfs for all three surface conditions at $Re_{cr} + 400$, $Re_{cr} + 600$, $Re_{cr} + 1,000$, and $Re_{cr} + 1,600$, respectively. At

Fig. 10 Probability density functions of $u'v'$ normalized by $|\langle u'v' \rangle|_{max}$ at $y = 0.25W$ for the **a** smooth, **b** R1, and **c** R2 cases

$Re_{cr} + 400$ (Fig. 11a), while the positive $u'v'$ events remain relatively unaffected by surface roughness, the negative tails of the $u'v'$ pdfs increase slightly with increasing surface roughness. With increasing Re, a greater skew toward negative values is noted and at $Re_{cr} + 600$ (Fig. 11b) this enhancement is clearly evident in the negative tails of the pdfs despite little change in their positive tails. This intensification of negative $u'v'$ events becomes progressively more apparent with increasing Re as the flow tends toward a turbulent state with the largest enhancement in ejection/sweep events noted for turbulent flow at $Re_{cr} + 1,600$ (Fig. 11d). Finally, while not obvious in the early stages of transition, a slight enhancement in positive $u'v'$ events is noted in the latter stages of transition (Fig. 11c) that continues to grow slowly as a turbulent state is reached (Fig. 11d). These pdfs therefore provide evidence of a progressive enhancement of ejection and/or sweep events with both Re and increasing surface roughness that in turn lead to the enhancement in the mean RSS noted in Fig. 9d.

In order to examine the relative contributions of u' and v' to the pdfs of RSS-producing $u'v'$ events, Fig. 12 shows joint pdfs of (u', v') computed at $y = 0.25W$ for $Re_{cr} + 600$. The joint pdf for the smooth-wall case (Fig. 12a) is elliptical in shape with its major axis rotated at a very slight angle away from the horizontal–consistent with the dominance of u' fluctuations in the generation of intense RSS-producing events (the magnitudes of the largest u' fluctuations are slightly less than two times the magnitudes of the largest v' fluctuations). With increasing surface roughness, while the joint pdf of (u', v') remains elliptical, a progressive skew is noted toward the second and fourth quadrants of the $u'-v'$ plane [$(u' < 0, v' > 0)$ and $(u' > 0, v' < 0)$, respectively] that induces rotation of the major axis further away from the horizontal. This skew with increasing roughness is predominantly due to a significant increase in the characteristic magnitude of v' as the characteristic magnitude of u' with increasing surface roughness remains relatively unaltered. As such, for fixed
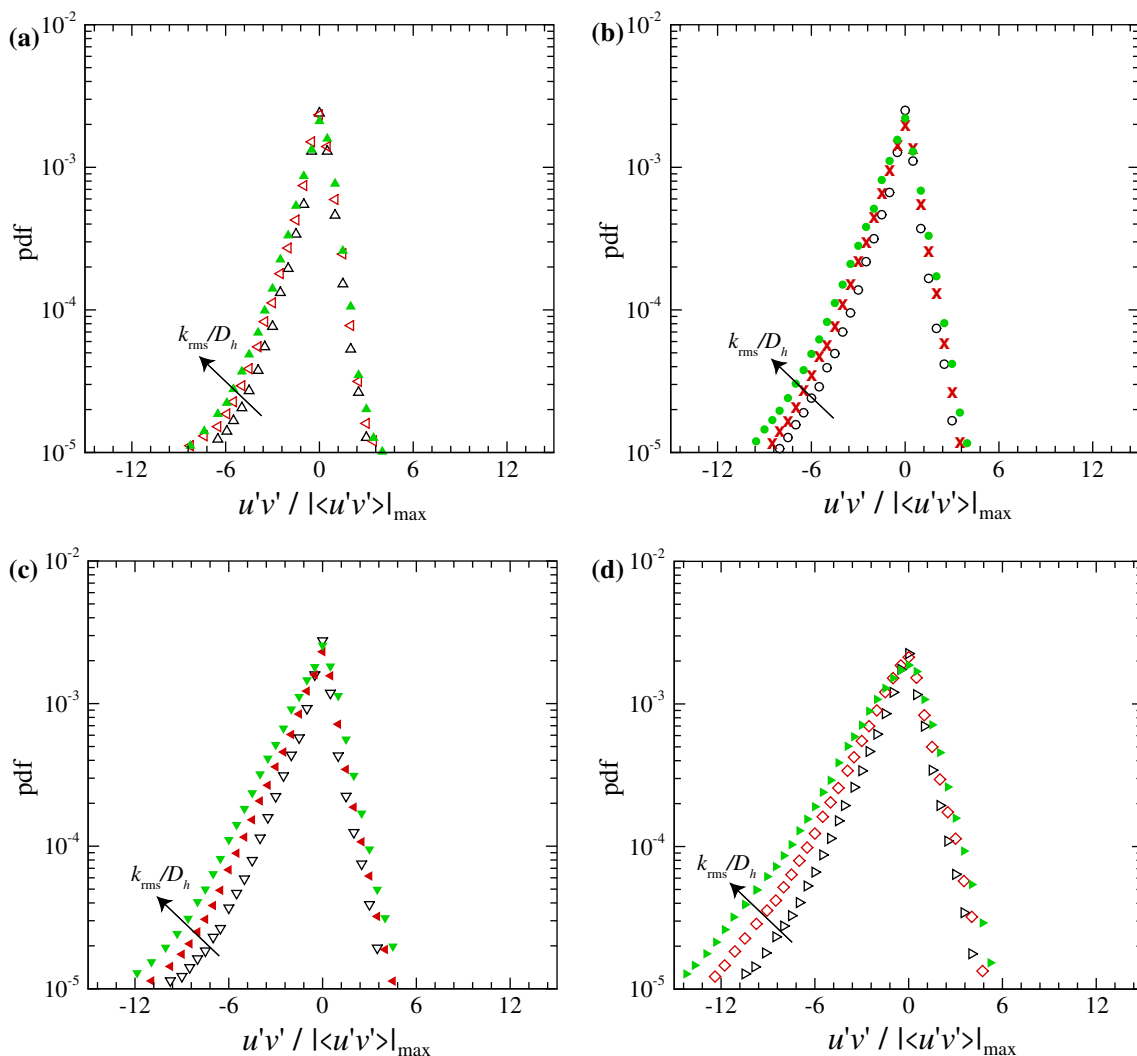
Fig. 11 Comparison of the probability density functions of $u'v'$ normalized by $|\langle u'v' \rangle|_{max}$ at $y = 0.25W$ for the smooth- and rough-wall cases at **a** $Re_{cr} + 400$, **b** $Re_{cr} + 600$, **c** $Re_{cr} + 1,000$, and **d** $Re_{cr} + 1,600$

$Re - Re_{cr}$ the growth in the magnitude of the mean RSS and in the number and/or intensity of negative RSS-producing events noted in the $u'v'$ pdfs with increasing roughness is predominantly attributable to an enhancement in the wall-normal velocity fluctuations by roughness.

4.2.6 Quadrant analysis

The pdfs presented in Figs. 10, 11, 12 suggest that surface roughness enhances the mean RSS via a progressive increase in the occurrence and/or strength of negative $u'v'$ events, particularly in the region closer to the wall ($y \lesssim 0.5W$), due predominantly to a significant enhancement in the v' fluctuations. However, it is not clear whether this enhancement in the mean RSS via negative $u'v'$ events is associated with an increased occurrence and/or strength of ejections, sweeps, or both, as these events both contribute heavily to the mean RSS. Therefore, quadrant

analysis, as introduced by Lu and Willmarth (1973), is employed to identify the dominant contributors to the roughness-induced enhancement of the mean RSS and document the Reynolds-number evolution of the wall-normal dependence of the $\langle u'v' \rangle$ profiles for the smooth- and rough-wall cases. In quadrant analysis, the mean RSS at each wall-normal position can be decomposed into contributions from four quadrants ($Q = 1-4$), excluding a hyperbolic hole of size H, as

$$\langle u'v' \rangle_Q (y; H) = \frac{1}{M} \sum_{j=1}^{M} u'(x_j, y) v'(x_j, y) I_Q(x_j, y; H), \qquad (9)$$

where the indicator function, I_Q, is defined as

$$I_Q(x_j, y; H) = \begin{cases} 1 & \text{when } |u'(x_j, y)v'(x_j, y)|_Q \geq H |\langle u'v' \rangle|_{max} \\ 0 & \text{otherwise,} \end{cases}$$

$$(10)$$
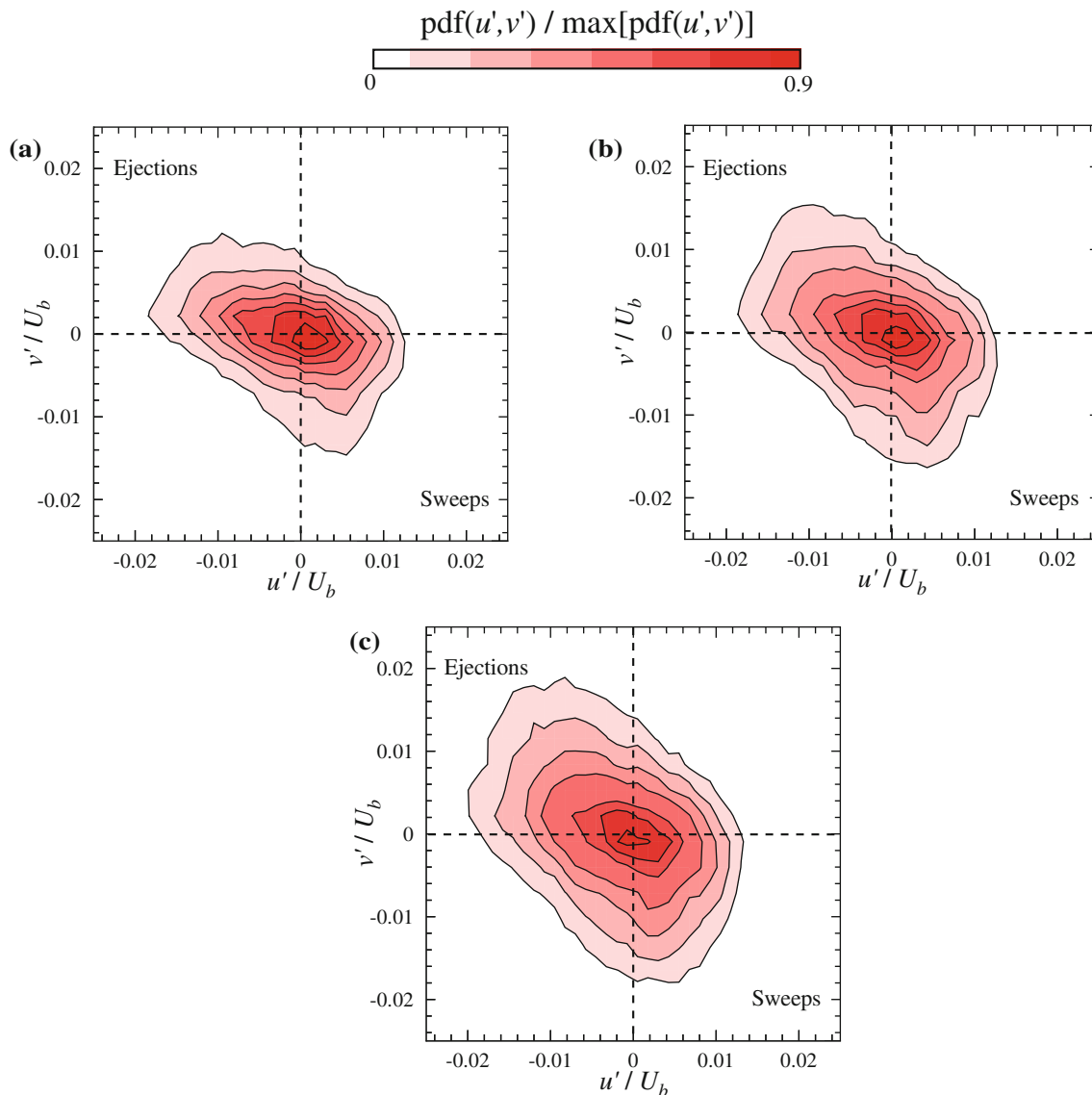
Fig. 12 Joint probability density functions of $(u'v')$ at $y = 0.25W$ for $Re_{cr} + 600$ for the **a** smooth, **b** R1, and **c** R2 cases

and M is the total number of grid points at each wall-normal position. In Eq. 10, H represents a non-zero hole size that acts as a threshold to exclude $u'v'$ events of small magnitude in order to determine the relative contributions of the more intense $u'v'$ events. In addition, the summation in Eq. 9 represents an ensemble average followed by a line average in the streamwise direction for a fixed wall-normal position.

Quadrant analysis yields two quantities that are of particular interest in assessing the contributions of ejections and sweeps to $\langle u'v' \rangle$ at different Re and surface conditions: the contributions of the aforementioned events to the mean RSS for a given H: $\langle u'v' \rangle_Q(y)$ (Eq. 9) and the fraction of space, $N_Q(y)$, occupied by each of the above events for a given H, defined as

$$N_Q(y; H) = \frac{\sum_{j=1}^{M} I_Q(x_j, y; H)}{M}. \tag{11}$$

The latter quantity provides a means of assessing whether more numerous intense $u'v'$ events are produced by surface roughness or whether the noted enhancement is simply due to stronger RSS-producing events. In order to achieve these goals, these quantities are computed for ejections and sweeps for hole sizes of $H = 0$ and 4—inclusion of all and only the most intense RSS-producing events, respectively, for the smooth, R1 and R2 cases. Inward and outward interactions are not included in the analysis since the pdfs in Figs. 10, 11, 12 suggest little impact of surface roughness on these events.

Figure 13a, b shows profiles of the RSS contributions from ejections and sweeps, $\langle u'v' \rangle_2$ and $\langle u'v' \rangle_4$,
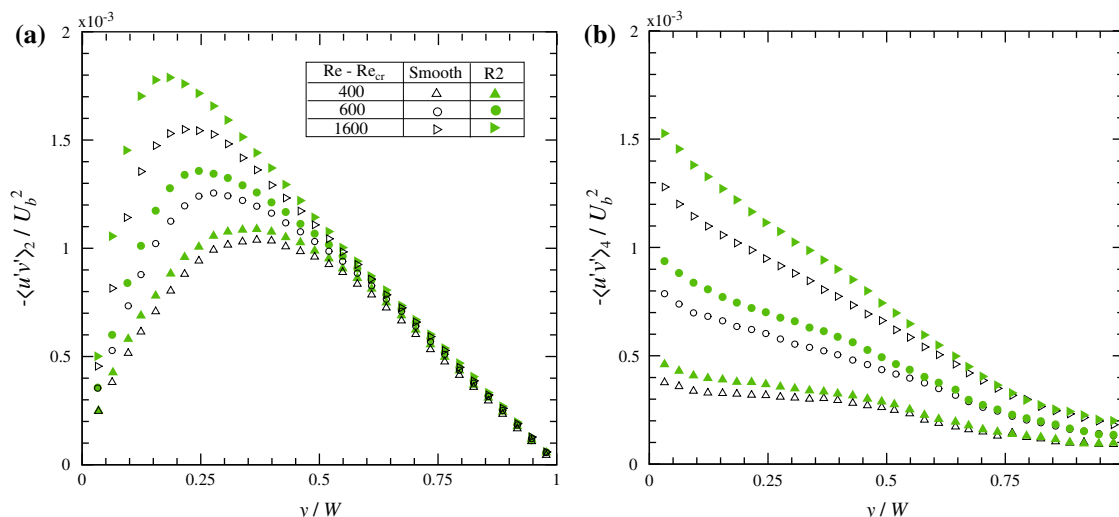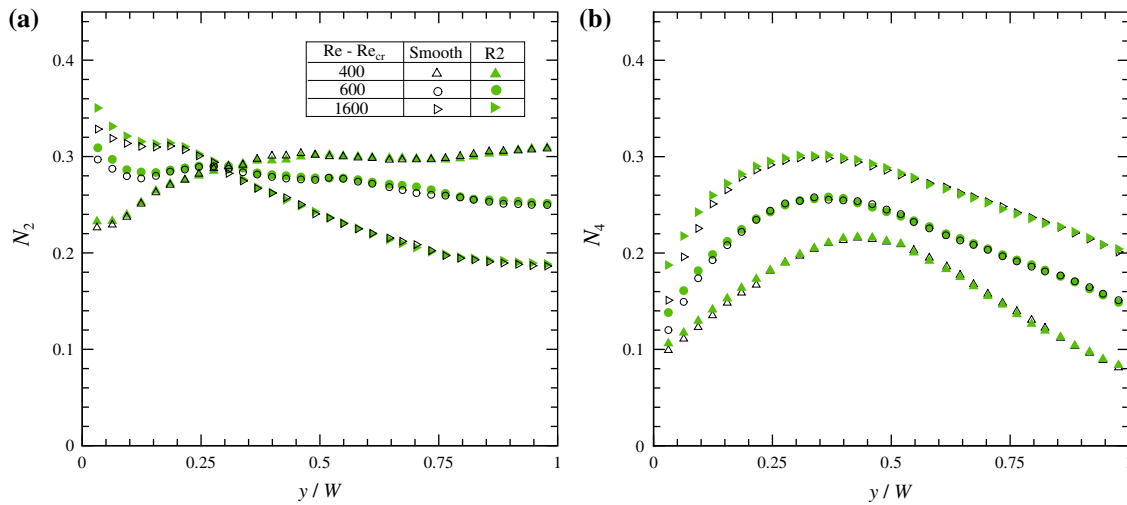
Fig. 13 Contributions of **a** ejections and **b** sweeps to the mean Reynolds shear stress versus wall-normal position for $H = 0$ at $Re_{cr} + 400$, $Re_{cr} + 600$ and $Re_{cr} + 1,600$

corresponding to $H = 0$ at $Re_{cr} + 400, Re_{cr} + 600$, and $Re_{cr} + 1,600$ for the smooth and R2 cases. The contributions for the R1 case at all wall-normal locations lie midway between that noted for the smooth and R2 cases and are therefore not presented for clarity. The case $H = 0$ implies that the contributions from all instantaneous $u'v'$ events are included, meaning $\langle u'v' \rangle_2$ and $\langle u'v' \rangle_4$ represent the total contributions of ejections and sweeps to the mean RSS profiles in Fig. 9d. For the smooth-wall case, Fig. 13a, b illustrates a progressive growth in the contributions from ejections and sweeps as the flow transitions toward a turbulent state with increasing Re. Consistent with the observations of Natrajan and Christensen (2009a) for smooth-wall capillary flow, while sweeps dominate over ejections in the immediate vicinity of the wall, ejections dominate beyond this region with the peak in ejection contributions shifting closer to the wall with increasing Re as was noted in the mean RSS profiles (Fig. 9d). Turning to the R2 case, while the wall-normal trends of $\langle u'v' \rangle_2$ and $\langle u'v' \rangle_4$ are qualitatively similar to those of smooth-wall flow, differences in the magnitudes of $\langle u'v' \rangle_2$ and $\langle u'v' \rangle_4$ are apparent in the region $y \lesssim 0.5W$ for fixed $Re - Re_{cr}$. In the case of ejection contributions (Fig. 13a), collapse in the smooth and R2 profiles is noted in the core of the flow $(y \gtrsim 0.5W)$ while enhancement in the ejection contributions is noted with increasing roughness as one moves closer to the wall. This enhancement attains a maximum at the wall-normal location where the peak in $\langle u'v' \rangle_2$ is observed. Similar trends are noted in the sweep contributions (Fig. 13b), where the roughness-induced enhancement is largest in the near-wall region and decreases as one moves away from the wall until collapse is noted near the centerline of the capillary for fixed $Re - Re_{cr}$. In both

cases, this roughness-induced enhancement grows substantially with increasing $Re - Re_{cr}$, which is consistent with the trends noted in the mean RSS profiles and the pdfs in Figs. 10, 11.

The space fractions of ejections and sweeps, N_2 and N_4, corresponding to $H = 0$ for the smooth and R2 cases are shown in Fig. 14a, b, respectively. For the smooth-wall case, consistent with the trends noted by Natrajan and Christensen (2009a) for smooth-wall capillary flow, N_2 increases from the capillary wall to the centerline at $Re_{cr} + 400$, while it shifts to being nearly constant and one of steady increase with increasing y at $Re_{cr} + 600$ and $Re_{cr} + 1,600$, respectively. In contrast, the wall-normal trends of the sweep space fraction, N_4, for the smooth-wall case (Fig. 14b) remain the same at all Re presented in that it increases in magnitude with increasing y, attains a peak, and subsequently decreases as the centerline is approached. Interestingly, for fixed $Re - Re_{cr}$, the R2 space fractions behave in a very similar manner with y compared to the smooth-wall results with collapse irrespective of surface condition noted everywhere except in the very near-wall region $(y/W \lesssim 0.1)$ where a weak roughness-induced enhancement is noted in both N_2 and N_4 that grows only slightly with increasing Re. Therefore, coupling these observations with the trends of $\langle u'v' \rangle_2$ and $\langle u'v' \rangle_4$, while roughness enhances the RSS contributions of both ejections and sweeps at fixed $Re - Re_{cr}$, the space occupied by these events remains relatively unaffected by roughness except in the immediate vicinity of the wall.

Figure 15 shows the contributions of ejections and sweeps to the mean RSS at a threshold of $H = 4$ for the smooth- and rough-wall cases which ensures that only the most intense instantaneous $u'v'$ events are included in

Fig. 14 Space fractions of **a** ejections and **b** sweeps versus wall-normal position for $H = 0$ at $Re_{cr} + 400$, $Re_{cr} + 600$, and $Re_{cr} + 1,600$
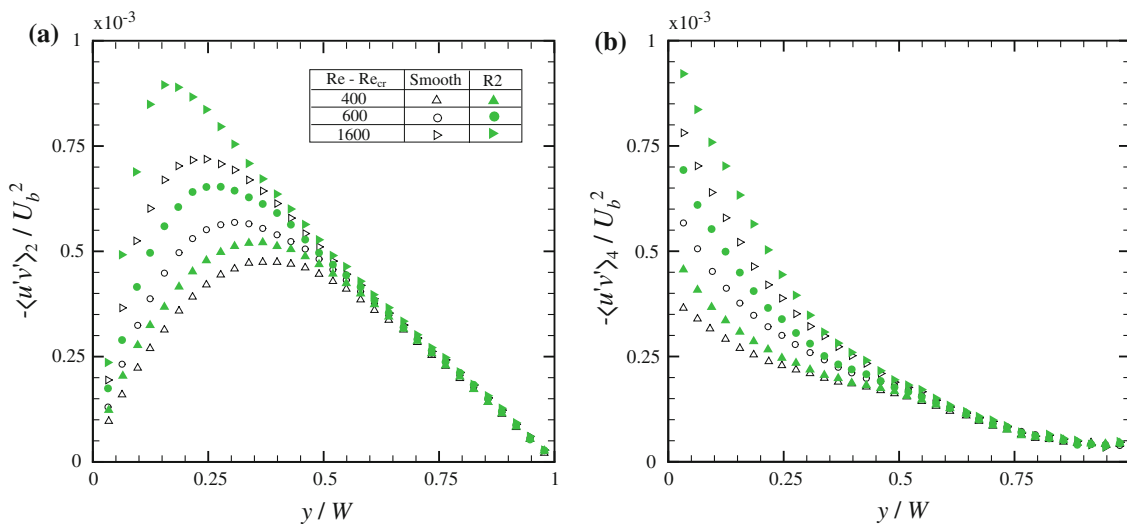
Fig. 15 As Fig. 13 except $H = 4$

the decomposition. The wall-normal trends of $\langle u'v' \rangle_2$ at $H = 4$ (Fig. 15a) are quite similar to the $H = 0$ profiles though the magnitude of $\langle u'v' \rangle_2$ decreases by about 50% for the $H = 4$ case due to the more stringent threshold. In addition, the roughness-induced enhancement in $\langle u'v' \rangle_2$ at fixed $Re - Re_{cr}$ for the $H = 4$ case is greater than that noted for the $H = 0$ case. Similar trends are noted in the wall-normal trends of $\langle u'v' \rangle_4$ for $H = 4$ (Fig. 15b), where an enhancement in $\langle u'v' \rangle_4$ is noted with increase in surface roughness for $y < 0.5W$ (where significant Re-dependence is noted). Finally, Fig. 16 shows the space fractions of the most intense ejection and sweep events for the smooth and R2 cases corresponding to $H = 4$. In contrast to the space-fraction results for $H = 0$ case where collapse of the smooth- and rough-wall results was noted except for a very weak enhancement close to the wall, the intense ejection

and sweep events corresponding to $H = 4$ are much more numerous for the R2 case compared to that noted for the smooth-wall case in the region $y < 0.35W$. As such, it appears that the roughness-induced enhancement of the mean RSS noted in Fig. 9d and the roughness-induced enhancement in the negative tails of the $u'v'$ pdfs is associated both with an enhancement in the intensity of ejection and sweep events, particularly intense events, as well as an increase in the number of extremely intense ejection and sweep event close to the wall. The occurrence of more numerous ejection events can be directly related back to the structural observations made earlier where roughness was found to generate larger populations of spanwise vortical structures, likely hairpin-like vortices, which directly induce such ejection events. In this way, the additional vortical structures generated with increasing
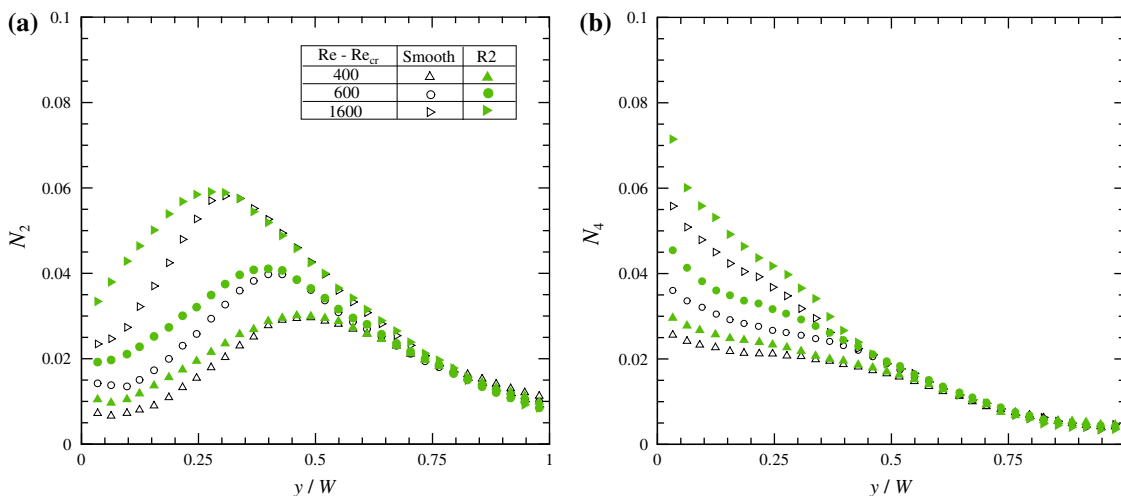
Fig. 16 As Fig. 14 except $H = 4$

roughness serve to enhance the energy content of the underlying disturbances (turbulent spots) which likely leads to the accelerated pathway toward a turbulent state observed in the laminar-fraction trends of Fig. 6.
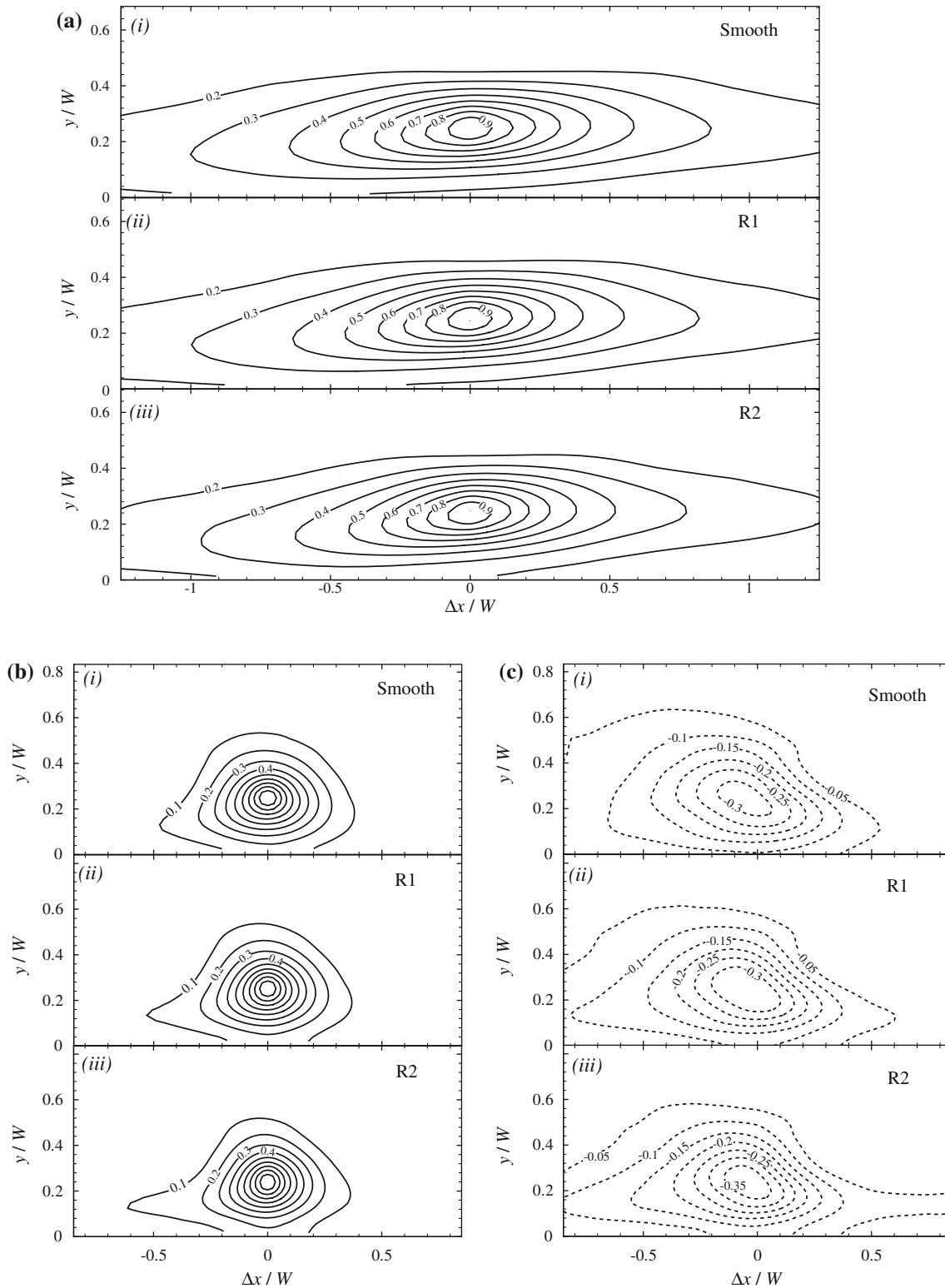
4.2.7 Two-point velocity correlations

Finally, since the single-point statistics reveal significant enhancement in the magnitudes of the velocity fluctuations with increasing surface roughness for transitional and turbulent flow, it is of interest to document the similarities and differences in the average spatial signatures of the underlying structures for the smooth- and rough-wall cases. From a structural viewpoint, it is well-established that spatial correlations of velocity embody imprints of the underlying structure of wall-bounded turbulent flows (Christensen and Adrian 2001; Liu et al. 2001; Christensen et al. 2004; Ganapathisubramani et al. 2005). In particular, these studies indicate that the long streamwise extent and slight inclination away from the wall of hairpin-vortex packets in wall-bounded turbulence are responsible for similar characteristics in the two-point correlation coefficient of streamwise velocity, ρ_{uu}, within the streamwise–wall-normal plane where

$$\rho_{ij}(\Delta x, y; y_{\text{ref}}) = \frac{\langle u_i'(x, y_{\text{ref}}) u_j'(x + \Delta x, y)\rangle}{\sigma_i(y_{\text{ref}})\sigma_j(y)}, \quad (12)$$

is the two-point velocity correlation coefficient tensor in the streamwise–wall-normal $(x-y)$ plane assuming homogeneity in the streamwise direction, Δx is the spatial separation in the streamwise direction, and σ_i is the RMS of the ith velocity component. Since the wall-normal direction is statistically inhomogeneous, ρ_{ij} is computed for all wall-normal locations, y, for a fixed reference location, y_{ref}.

Figure 17a–c shows the two-point velocity correlation coefficients, ρ_{uu}, ρ_{vv}, and ρ_{uv}, respectively, for $y_{\text{ref}} = 0.25W$, computed at $Re_{\text{cr}} + 600$ for the smooth, R1 and R2 cases, respectively. As should be expected based upon previous macroscale studies and correlations reported by Natrajan and Christensen (2009a) for transitional smooth-wall capillary flow, the two-point correlation coefficient of streamwise velocity, ρ_{uu}, is elongated in the streamwise direction and inclined slightly away from the wall for all three surface conditions. These spatial characteristics are consistent with the elongated, yet slightly inclined, regions of streamwise momentum deficit noted in the instantaneous velocity fields of Fig. 7 and can therefore be interpreted as the statistical imprint of instantaneous hairpin-vortex packets (Christensen et al. 2004; Ganapathisubramani et al. 2005). Since these qualitative patterns exist irrespective of surface condition, it appears that the present surface roughness under consideration does not appreciably alter the overall structural paradigm of transitional and turbulent flow in microchannels. Despite these qualitative consistencies, subtle differences between the smooth- and rough-wall ρ_{uu} are apparent, including a slight shortening in the streamwise extent of ρ_{uu} with increasing surface roughness. For instance, the streamwise extent associated with $\rho_{uu} = 0.3$ at $y = y_{\text{ref}}$ is $1.87W$, $1.80W$ and $1.72W$ for the smooth, R1 and R2 cases, respectively. Further, the inclination angle of ρ_{uu} increases slightly with increasing surface roughness, from nearly zero for the smooth-wall case to approximately 4° for the rough-wall case. As such, these trends in ρ_{uu} may reflect the possibility that the organization of vortex packets becomes slightly more compact with more noted inclination away from the wall with increasing surface roughness. Another explanation for the observed shortening in ρ_{uu} with increasing surface roughness may be offered in terms of recent observations

Fig. 17 Two-point velocity correlation coefficients at $y_{\text{ref}} = 0.25W$ for the smooth, R1 and R2 cases at $Re_{\text{cr}} + 600$. **a** ρ_{uu}; **b** ρ_{vv}; **c** ρ_{uv}

that hairpin-vortex packets in macroscale wall turbulence can meander significantly in the spanwise direction of the flow (Hutchins and Marusic 2007). Such meandering can

greatly reduce the streamwise extent of ρ_{uu} in macroscale wall turbulence since for a measurement plane fixed at a given spanwise location (as is the case herein), this

meandering would cause these motions to appear and disappear within this plane with some streamwise frequency, effectively reducing their apparent streamwise extent. As such, the possibility of this effect increasing with surface roughness and thereby resulting in the shortening of ρ_{uu} noted herein cannot be discounted. Nevertheless, this shortening of ρ_{uu} in the present roughness cases for the non-laminar subsets is entirely consistent with previous observations in macroscale studies of rough-wall turbulence (Nakagawa and Hanratty 2001; Volino et al. 2007; Wu and Christensen 2007).

The two-point correlation coefficient of the wall-normal velocity, ρ_{vv}, on the other hand, is much more compact in the streamwise direction reflecting the imprint of individual spanwise vortices (Christensen et al. 2004). In general, while a slight increase is noted in the streamwise extent associated with $\rho_{vv} = 0.1$ with increasing surface roughness, the wall-normal extent of ρ_{vv} appears relatively insensitive to the presence of roughness. Finally, Fig. 12c shows ρ_{uv} for the three surface conditions and it is found to embody spatial scales intermediate to that of the ρ_{uu} and ρ_{vv}. It should be noted that ρ_{uv} is negative everywhere, meaning that positive u' are generally spatially correlated with negative v' and vice-versa which is consistent with the u' and v' combinations that form ejection and sweep contributions to the mean RSS. Of interest, ρ_{uv} becomes slightly more compact with increasing roughness and its value increases near the reference location ($\Delta x \approx 0$ and $y \approx y_{ref}$). This behavior is consistent with the aforementioned observations of increased magnitudes of ejection and sweep events. Therefore, these correlations indicate that while roughness can induce subtle differences in the average spatial characteristics of the underlying structure, it does not alter the overall structural paradigm of smooth-wall transitional and turbulent flow in the microchannel.

5 Summary

The present effort details the impact of surface roughness on the flow characteristics within a rectangular microchannel of hydraulic diameter $D_h = 600 \, \mu m$ (wherein two of the four microchannel walls are roughened) in the laminar, transitional, and turbulent regimes using both pressure-drop measurements and instantaneous velocity fields acquired by micro-PIV. The roughness considered is unique in that it embodies a broad range of topographical scales meant to mimic surface irregularities one might encounter in microscale flow passages due to fabrication imperfections. The pressure-drop measurements conducted across the length of the copper microchannel reveal the onset of transition above $Re_{cr} \cong 1,800$ for the smooth-wall case, which is consistent with similar processes at the

macroscale. In contrast, deviation from laminar behavior is noted above $Re_{cr} \cong 1,500$ and $1,300$ for two rough-wall cases, R1 and R2, respectively, with R2 rougher than R1. These observations are consistent with mean velocity profiles calculated from data sets acquired in the transitional regime for the smooth- and rough-wall cases that illustrate deviation from fully developed laminar behavior for $Re > Re_{cr}$. As such, previous studies of supposedly smooth-wall microscale flow passages indicating an early onset of transition, but for which details regarding the internal surface quality of the passages were not reported, may have in fact suffered from roughness effects. With increasing Re, the mean velocity profiles for the smooth- and rough-wall cases become progressively flatter and fuller in character which is indicative of a gradual progression of the flow toward a turbulent state. In addition, comparison of the mean velocity profiles at $Re - Re_{cr}$ reveals larger velocity gradients in the region close to the wall with increasing surface roughness that are consistent with larger values of the wall shear stress in the presence of increasing roughness as was noted in the pressure-drop measurements.

Of particular interest, there exists a hastening of a flow toward a turbulent state even when referencing these processes relative to the onset of transition at Re_{cr} which decreases with increasing roughness. This hastening is most notable in the early stages of transition where the growth in the fraction of velocity fields exhibiting disordered motion grows dramatically with increasing surface roughness. This disparity reduces as a turbulent state is approached until all three surface conditions reach a turbulent state at roughly $Re - Re_{cr} = 1,600$, meaning that, while there exists an acceleration in the early transition processes with increasing roughness, the range of Re over which the flow transitions from a laminar to a turbulent state is essentially the same irrespective of surface condition. Despite these differences, instantaneous velocity realizations exhibiting disordered motion for the different surface conditions indicate little impact of roughness on the overall structural paradigm of transitional and turbulent smooth-wall flow. In particular, these fields support the existence of multiple hairpin-like vortices that appear streamwise-aligned to form large-scale vortex packets, akin to that noted in both transitional and turbulent flow at the micro- and macro-scales. However, closer examination of these fields also reveals a noted increase in the intensity of the underlying velocity fluctuations accompanied by more numerous vortical structures with increasing surface roughness. These trends are supported by profiles of the single-point statistics of the velocity fluctuations of the non-laminar ensembles, including profiles of the RMS streamwise and wall-normal velocities and the Reynolds shear stress, and pdfs of the RSS-producing $u'v'$ events

which show an increase in the number of negative $u'v'$ with increasing roughness in the region close to the wall. These trends, along with quadrant analysis, indicate that this enhancement in RSS is due primarily to a substantial growth in the characteristic magnitude of the wall-normal velocity fluctuations with increasing Re and roughness.

References

Adrian RJ, Christensen KT, Liu ZC (2000a) Analysis and interpretation of instantaneous turbulent velocity fields. Exp Fluids 29:275–290

Adrian RJ, Meinhart CD, Tomkins CD (2000b) Vortex organization in the outer region of the turbulent boundary layer. J Fluid Mech 422:1–54

Christensen KT (2004) The influence of peak-locking errors on turbulence statistics computed from PIV ensembles. Exp Fluids 36:484–497

Christensen KT, Adrian RJ (2001) Statistical evidence of hairpin vortex packets in wall turbulence. J Fluid Mech 431:433–443

Christensen KT, Adrian RJ (2002) Measurement of instantaneous eulerian acceleration fields by particle-image accelerometry: method and accuracy. Exp Fluids 33:759–769

Christensen KT, Wu Y, Adrian RJ, Lai W (2004) Statistical imprints of structure in wall turbulence. AIAA paper 2004-1116

Colebrook CF (1939) Turbulent flow in pipes with particular reference to the transition region between the smooth- and rough-pipe laws. J Inst Civil Eng 11:133–156

Colebrook CF, White CM (1937) Experiments with fluid friction in roughened pipes. Proc R Soc Lond A 161:367–381

Darbyshire AG, Mullin T (1995) Transition to turbulence in a constant-mass-flux pipe flow. J Fluid Mech 289:83–114

Eggels JGM, Unger F, Weiss MH, Westerweel J, Adrian RJ, Friedrich R, Nieuwstadt FTM (1994) Fully developed turbulent pipe flow: a comparison between direct numerical simulation and experiment. J Fluid Mech 268:175–209

Ergu OB, Sara ON, Yapici S, Arzutugu ME (2009) Pressure drop and point mass transfer in a rectangular microchannel. Int Commun Heat Mass Transf 36(6):618–623

Ganapathisubramani B, Longmire EK, Marusic I (2003) Characteristics of vortex packets in turbulent boundary layers. J Fluid Mech 478:35–46

Ganapathisubramani B, Hutchins N, Hambleton WT, Longmire EK, Marusic I (2005) Investigation of large-scale coherence in a turbulent boundary layer using two-point correlations. J Fluid Mech 524:57–80

Hao PF, Yao ZH, He F, Zhu KQ (2006) Experimental investigation of water flow in smooth and rough silicon microchannels. J Micromech Microeng 16:1397

Hsieh SS, Lin CY, Huang CF, Tsai HH (2004) Liquid flow in a microchannel. J Micromech Microeng 14:436–445

Hutchins N, Marusic I (2007) Evidence of very long meandering features in the logarithmic region of turbulent boundary layers. J Fluid Mech 579:1–28

Idelchick IE (1986) Handbook of hydraulic resistance, chap 2. Hemisphere, New York

Jones OC (1976) An improvement in the calculation of turbulent friction in rectangular ducts. J Fluids Eng 98:173–181

Judy J, Maynes D, Webbs BW (2002) Characterization of frictional pressure drop for liquid flows through microchannels. Int J Heat Mass Transf 45:3477–3489

Kandlikar SG, Schmitt D, Carrano AL, Taylor JB (2005) Characterization of surface roughness effects on pressure drop in single-phase flow in minichannels. Phys Fluids 17:100606

Kline SJ, Robinson SK (1989) Quasi-coherent structures in the turbulent bounday layer. Part 1: status report on a community-wide summary of the data. Hemisphere, New York, pp 218–247

Li H, Olsen MG (2006a) Examination of large-scale structures in turbulent microchannel flow. Exp Fluids 40:733–743

Li H, Olsen MG (2006b) Aspect ratio effects in turbulent and transitional flow in rectangular microchannels as measured with micro-PIV. J Fluids Eng 128:305–315

Li H, Ewoldt R, Olsen MG (2005) Turbulent and transitional velocity measurements in a rectangular microchannel using microscopic particle image velocimetry. Exp Therm Fluid Sci 29:435–446

Liu ZC, Adrian RJ, Hanratty TJ (2001) Large-scale modes of turbulent channel flow: transport and structure. J Fluid Mech 448:53–80

Liu Z, Zhang C, Huo Y, Zhao X (2007) Flow and heat transfer in rough micro steel tubes. Exp Heat Transf 20:289–306

Lu SS, Willmarth WW (1973) Measurements of the structure of Reynolds stress in a turbulent boundary layer. J Fluid Mech 60:481–511

Mala GM, Li D (1999) Flow characteristics of water in microtubes. Int J Heat Fluid Flow 20:142–148

Meinhart CD, Wereley ST, Santiago JG (2000) PIV measurements of a microchannel flow. Exp Fluids 27:414–419

Moody LF (1944) Friction factors for pipe flow. Trans ASME 66:671

Morini GL (2004) Laminar-to-turbulent flow transition in microchannels. Microscale Thermophys Eng 8(1):15–30

Nakagawa S, Hanratty TJ (2001) Particle image velocimetry measurements of flow over a wavy wall. Phys Fluids 13(11):3504–3507

Natrajan VK, Christensen KT (2007) Microscopic particle image velocimetry measurements of transition to turbulence in microscale capillaries. Exp Fluids 43:1–16

Natrajan VK, Christensen KT (2009a) Structural characteristics of transition to turbulence in microscale capillaries. Phys Fluids 21 (034104)

Natrajan VK, Christensen KT (2009b) Non-intrusive measurements of convective heat transfer in smooth- and rough-wall microchannels. Part I: laminar flow. Exp Fluids (submitted)

Natrajan VK, Christensen KT (2009c) Non-intrusive measurements of convective heat transfer in smooth- and rough-wall microchannels. Part II: transitional and turbulent flow. Exp Fluids (submitted)

Natrajan VK, Yamaguchi E, Christensen KT (2007) Statistical and structural similarities between micro- and macro-scale wall turbulence. Microfluid Nanofluid 3:89–100

Nikuradse J (1933) Laws of flow in rough pipes. NACA Technical Memorandum (1292)

Obot NT (1988) Determination of incompressible flow friction in smooth circular and noncircular passages: a generalized approach including validation of the nearly century old hydraulic concept. J Fluids Eng 110:431–440

Olsen MG, Adrian RJ (2000) Out-of-focus effects on particle image visibility and correlation in microscopic particle image velocimetry. Exp Fluids 29:S166–S174

Peng XF, Peterson GP (1996) Convective heat transfer and flow friction for water flow in microchannel structures. Int J Heat Mass Transf 39:2599–2608

Peng XF, Peterson GP, Wang BX (1994) Frictional flow characteristics of water flowing through rectangular microchannels. Exp Heat Transf 7:249–264

Pfund D, Rector D, Shekarriz A, Popescu A, Welty J (2000) Pressure drop measurements in a microchannel. AIChE J 46:1496–1507

Prasad AK, Adrian RJ, Landreth CC, Offutt PW (1992) Effect of resolution on the speed and accuracy of particle image velocimetry interrogation. Exp Fluids 13:105–116

Qi SL, Zhang P, Wang RZ, Xu LX (2007) Single-phase pressure drop and heat transfer characteristics of turbulent liquid nitrogen flow in micro-tubes. Int J Heat Mass Transf 50(9–10):1993–2001

Qu W, Mudawar I (2002) Experimental and numerical study of pressure drop and heat transfer in a single-phase micro-channel heat sink. Int J Heat Mass Transf 45:2549–2565

Qu W, Mala GM, Li D (2000) Pressure driven water flows in trapeziodal silicon microchannels. Int J Heat Fluid Flow 43:353–364

Reynolds O (1883) An experimental investigation of circumstances which determine whether the motion of water shall be direct or continuous, and the law of resistance in parallel channels. Philos Trans R Soc Lond 174:935–982

Santiago JG, Wereley ST, Meinhart CD, Beebe DJ, Adrian RJ (1998) A particle image velocimetry system for microfluidics. Exp Fluids 25:316–319

Schlichting H (1979) Boundary-layer theory. McGraw-Hill, New York

Schröder A, Kompenhans J (2004) Investigation of a turbulent spot using multi-plane stereo particle image velocimetry. Exp Fluids 36:82–90

Shah RK, London AL (1978) Laminar flow forced convection in ducts (Advances in heat transfer, supplement 1). Academic Press, New York

Sharp KV, Adrian RJ (2004) Transition from laminar to turbulent flow in liquid filled microtubes. Exp Fluids 36:741–747

Volino RJ, Schultz MP, Flack KA (2007) Turbulence structure in rough- and smooth-wall boundary layers. J Fluid Mech 592:263–293

Wang BX, Peng XF (1994) Experimental investigation on liquid forced-convection heat transfer through microchannels. Int J Heat Mass Transf 37:73–82

Westerweel J (1997) Fundamentals of digital particle image velocimetry. Meas Sci Technol 8:1379–1392

Wu P, Little W (1984) Measuring of heat transfer characteristics of gas flow in fine channel heat exchangers for micro miniature refrigerators. Cryogenics 24:415–420

Wu Y, Christensen KT (2007) Outer-layer similarity in the presence of a practical rough-wall topography. Phys Fluids 19:085108

Wygnanski IJ, Champagne FH (1973) On transition in a pipe. Part 1. The origin of puffs and slugs and the flow in a turbulent slug. J Fluid Mech 59:281–335

Wygnanski IJ, Sokolov M, Friedman D (1975) On transition in a pipe. Part 2. The equilibrium puff. J Fluid Mech 69:283–304

Yang CY, Wu JC, Chien HT, Lu SR (2003) Friction characteristics of water, R134a, and air in small tubes. Microscale Thermophys Eng 7:335–348

Zhou J, Adrian RJ, Balachandar S, Kendall TM (1999) Mechanisms for generating coherent packets of hairpin vortices in channel flow. J Fluid Mech 387:353–396